

## On the wake structure in streaming complex plasmas

This article has been downloaded from IOPscience. Please scroll down to see the full text article.

2012 New J. Phys. 14 053016

(<http://iopscience.iop.org/1367-2630/14/5/053016>)

View [the table of contents for this issue](#), or go to the [journal homepage](#) for more

Download details:

IP Address: 129.242.167.165

The article was downloaded on 06/09/2012 at 10:30

Please note that [terms and conditions apply](#).

## On the wake structure in streaming complex plasmas

Patrick Ludwig<sup>1,4</sup>, Wojciech J Miloch<sup>2,3</sup>, Hanno Kählert<sup>1</sup>  
and Michael Bonitz<sup>1</sup>

<sup>1</sup> Institut für Theoretische Physik und Astrophysik,  
Christian-Albrechts-Universität zu Kiel, 24098 Kiel, Germany

<sup>2</sup> Department of Physics, University of Oslo, Box 1048, Blindern,  
0316 Oslo, Norway

<sup>3</sup> Department of Physics and Technology, University of Tromsø,  
9037 Tromsø, Norway

E-mail: [ludwig@theo-physik.uni-kiel.de](mailto:ludwig@theo-physik.uni-kiel.de)

*New Journal of Physics* **14** (2012) 053016 (29pp)

Received 22 December 2011

Published 15 May 2012

Online at <http://www.njp.org/>

doi:10.1088/1367-2630/14/5/053016

**Abstract.** The theoretical description of complex (dusty) plasmas requires multiscale concepts that adequately incorporate the correlated interplay of streaming electrons and ions, neutrals and dust grains. Knowing the effective dust–dust interaction, the multiscale problem can be effectively reduced to a one-component plasma model of the dust subsystem. The goal of this paper is a systematic evaluation of the electrostatic potential distribution around a dust grain in the presence of a streaming plasma environment by means of two complementary approaches: (i) a high-precision computation of the dynamically screened Coulomb potential from the dynamic dielectric function and (ii) full 3D particle-in-cell simulations, which self-consistently include dynamical grain charging and nonlinear effects. The range of applicability of these two approaches is addressed.

<sup>4</sup> Author to whom any correspondence should be addressed.

**Contents**

<b>1. Introduction</b>	<b>2</b>
1.1. Plasma parameters	4
1.2. Grain charging and wake formation	4
<b>2. Linear response approach</b>	<b>6</b>
2.1. Theoretical approach	6
2.2. Numerical implementation	7
2.3. Results	8
<b>3. Three-dimensional particle-in-cell simulations</b>	<b>14</b>
3.1. Theoretical approach	15
3.2. Numerical implementation	15
3.3. Results	16
<b>4. Method-spanning comparison</b>	<b>22</b>
4.1. Comparison of the potentials	22
4.2. Consideration of shadowing effects	23
4.3. Range of applicability of both simulation models	25
<b>5. Summary and outlook</b>	<b>26</b>
<b>Acknowledgment</b>	<b>27</b>
<b>References</b>	<b>27</b>

**1. Introduction**

Complex (dusty) plasmas have been proven to be an instructive reference system for strong coupling and correlation effects [1–3]. Thereby, complex plasma research inherently connects key issues from several fields including low-temperature physics, warm dense matter physics, surface and solid-state physics, as well as material science [4–9].

The first-principles description of complex plasmas is a theoretically challenging problem. A dusty plasma consists of electrons, positive ions, neutral atoms and micrometer-sized dust grains, i.e. components with distinct mass asymmetry giving rise to dynamics on very different spatial and temporal scales. This multi-scale behavior, combined with the *non-ideal character* of a complex plasma, makes a full temporal resolution on all scales a numerically unfeasible task with current computer technology. However, there are two numerical approaches that can address the challenges associated with the complex plasma system: the one-component plasma (OCP) model and the particle-in-cell (PIC) method.

The OCP approach relies on the idea of reducing the quasi-neutral, multi-component complex plasma to a subsystem of dust grains, which interact via a screened Coulomb potential. In particular, the statically screened (Yukawa-type) potential yields good agreement with the experiments for various specific setups; see, for example, [10, 11]. Also, this isotropic potential is well suited for fundamental analytical and numerical investigations on cooperative effects such as self-organized structure formation [3, 12], collective dynamical processes [13–15], spectral properties [16, 17] or the melting behavior [18, 19] in strongly correlated (screened) Coulomb systems. The multi-component and non-equilibrium nature of a complex plasma requires, however, a careful analysis of plasma streaming and dynamical grain charging effects,

which were experimentally shown to become of utmost importance at least near the plasma sheath; see, for example, [20–25]. In a plasma with ions streaming at a uniform velocity, the dust potential becomes (strongly) anisotropic and takes the form of an oscillatory wake structure in the downstream direction, which was the subject of various analytical and numerical studies, e.g. [26–42]<sup>5</sup>. This wake can result in attractive, non-reciprocal forces between the equally charged dust grains and lead to remarkable structural and dynamical consequences [43–49, 51, 52]. Streaming effects can be incorporated into the OCP dynamical screening model by means of linear response (LR) theory, as presented in section 2.

The second powerful numerical ansatz to tackle the multi-scale problem of the different plasma components is the PIC approach, in which the trajectories of plasma particles are followed in electric fields self-consistently [55]. To obtain a self-consistent charge on the grains, the plasma dynamics need to be resolved in the vicinity of the grain on spatial and temporal scales which are smaller than the Debye length and electron plasma period, respectively. However, due to the large mass of the grains (as compared to electrons and ions) as well as the large distances between the grains, the study of the dynamics of several dust grains requires simulation times that are much longer than the dust charging (which is on the ion plasma period time scale). Thus, a self-consistent 3D PIC calculation, i.e. a dynamic evolution of the three-dimensional (3D) system with more than one dust grain with a temporal resolution on the electron or ion plasma period time scale, required to ensure self-consistency, easily exceeds the capabilities of current high-performance computing systems [51, 56].

Consequently, short-time, small-scale PIC simulations of dust charging or, alternatively, less demanding LR calculations of the dynamical plasma shielding have to be coupled with large-scale OCP simulations which incorporate the interaction between the grains on a more abstract level [46–48]. Such a coupled multi-scale numerical approach may ensure the description of the correlated system dynamics with proper charges on the grains as well as an accurate potential distribution in the vicinity of grains. With the goal to form a method-spanning picture, the present paper comprises a systematic analysis of the electrostatic potential distribution around a dust grain in the presence of a streaming plasma environment by

1. a high-precision computation of the dynamically screened Coulomb potential from the dynamic dielectric function, and
2. a critical assessment of these LR results in particular with regard to nonlinear effects and dynamical grain charging processes by means of self-consistent 3D PIC simulations.

The discussion of the LR results in section 2 extends over a broad range of plasma streaming velocities and different electron-to-ion temperature ratios and includes an evaluation of the influence of collisional damping. The corresponding 3D PIC simulations in section 3 are performed for the collisionless limit and apply therefore to the low-pressure limit. Finally, it is vital to verify whether and to what extent the results obtained by a linear superposition of single-grain potentials coincide with the corresponding full 3D PIC simulations. Such a direct comparison is made for the case of two grains in section 4.

<sup>5</sup> For a review of previous experimental and theoretical works on the structure of the dust (wake) potential, see the following in-depth works [5–7, 23, 53, 54]. A recommended critical discussion of previous theoretical work on the structure of plasma wakes can be found in [42].

### 1.1. Plasma parameters

The plasma parameters are scaled to relevant base units, which are, in our case, the Debye length  $\lambda_{D\alpha} = \sqrt{\varepsilon_0 k_B T_\alpha / (n_\alpha q_\alpha^2)}$  and the plasma period  $\tau_\alpha = 2\pi / \omega_{p\alpha}$ , with the corresponding plasma frequency  $\omega_{p\alpha} = \sqrt{n_\alpha q_\alpha^2 / (\varepsilon_0 m_\alpha)}$ , where  $\alpha$  denotes electrons (e) or ions (i).  $T_\alpha$  is the corresponding temperature,  $n_\alpha$  density,  $m_\alpha$  mass,  $q_\alpha$  charge,  $k_B$  the Boltzmann constant and  $\varepsilon_0$  the permittivity of vacuum. The relative streaming velocity  $\mathbf{u}_i$  of the ions with respect to the dust is characterized by the Mach number  $M \equiv u_i / c_s$ , where the ion sound (Bohm) speed is given by  $c_s \equiv \sqrt{k_B T_e / m_i}$ . Furthermore, the thermal velocity is  $v_{T\alpha} = \sqrt{k_B T_\alpha / m_\alpha}$ .

The dynamically screened dust potential and in particular the characteristics of the wake are studied with respect to three dimensionless plasma parameters:

- the ion drift velocity, expressed in terms of the Mach number  $M$ ,
- the electron-to-ion temperature ratio  $T_r \equiv T_e / T_i$ ,
- the ion–neutral scattering frequency (normalized to the ion plasma frequency)  $\nu_{in} / \omega_{p_i}$ .

While the temperature ratio  $T_e / T_i$  controls the effect of Landau damping, the frequency ratio  $\nu_{in} / \omega_{p_i}$  determines the effect of collisional damping and can be effectively controlled in experiments by changing the neutral gas pressure. A simple approximation for the pressure as a function of the ion–neutral collision frequency and ion temperature is given by

$$p = \frac{\nu_{in} / \omega_{p_i} \cdot e_0 \sqrt{k_B T_i \cdot n_e / \varepsilon_0}}{\sigma_{in}}, \quad (1)$$

where  $e_0 = 1.602 \times 10^{-19}$  C is the elementary charge, and  $\sigma_{in} \simeq 5.0 \times 10^{-19}$  m<sup>2</sup> is the ion–neutral collision cross-section as defined in [57]<sup>6</sup>.

For the LR calculations, we consider argon, which is a typical working gas in complex plasma experiments [8]. The ions are considered to be singly charged ( $q_i = e_0$ ). Consequently, ion and electron densities are equal, and are set to  $n_e = n_i = 2.0 \times 10^{14}$  m<sup>-3</sup> and are considered as spatially homogeneous distributions. The considered electron temperature is  $T_e = 2.585$  eV ( $\simeq 30\,000$  K). The corresponding electron Debye length is  $\lambda_{D_e} = 845$   $\mu$ m. An atomic mass of argon  $m_n = m_i = 6.634 \times 10^{-26}$  kg leads to the Bohm speed of  $c_s = 2500$  m s<sup>-1</sup>. For the considered set of parameters, the ion plasma frequency takes the value of  $\omega_{p_i} = 3.0 \times 10^6$  Hz. For the PIC simulations, we simulate ions with a reduced mass  $m_i / m_e = 120$ , and thus  $\omega_{p_i}$  and  $c_s$  are increased accordingly (for details see section 3.1). Note that the LR and PIC results presented in this paper do not involve any kind of free fit parameters.

### 1.2. Grain charging and wake formation

The dust grains are charged by plasma currents and other currents, such as those induced by the photoelectric effect or secondary electron emission. For the charge equilibrium, the net current to the grain is zero, and such a grain is at *floating* potential  $\Phi_{fl}$  with respect to the surrounding plasma. If charging is only due to plasma currents (i.e. electron and ion fluxes to the surface), then in electropositive plasmas, the charge  $Q_d$  on the grain and the floating potential will be negative, due to the high mobility of electrons. The floating potential on a spherical, finite-sized

<sup>6</sup> We should note that the ion–neutral scattering frequency  $\nu_{in}$  and not the roughly approximated pressure  $p$  is used as input parameter for the LR calculations. For the energy dependence of the ion–neutral cross-section in argon, see, e.g., [58].

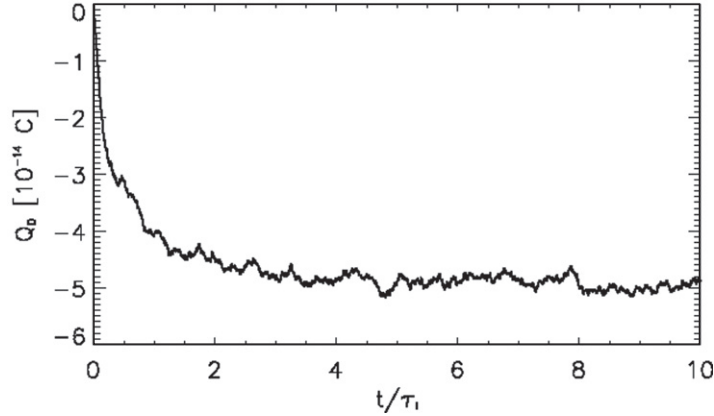


**Figure 1.** Typical charging characteristics for a spherical conducting grain in stationary plasma. Data are from 3D PIC simulations of a stationary plasma with  $T_e/T_i = 30$ ; time  $t$  is normalized to the ion plasma period  $\tau_i$ .

grain can be approximated with the orbit–motion–limited (OML) approach for both stationary and flowing collisionless plasmas [51]. We note that in the presence of collisions, the OML theory can give incorrect results, as has been noted by several authors [59–61]. The presence of trapped ions created by ion–neutral collisions can increase the ion current to the grain, and thus reduce the charge on the grain [62–64].

In a stationary plasma, the charging of a grain takes approximately one ion plasma period,  $\tau_i$ , a time in which the ions can collectively respond to the perturbations in the electric field. A typical charging characteristic for a single, spherical conducting grain is shown in figure 1, where the data are taken from 3D PIC simulations for the stationary plasma with  $T_e/T_i = 30$ . In the static case, the charge on a small grain can be calculated with the capacitance model for a given floating potential [65]:

$$Q_d = 4\pi\epsilon_0 a \left( 1 + \frac{a}{\lambda_D} \right) \Phi_{fl}, \quad (2)$$

where  $a$  is the grain radius and  $\lambda_D$  the total Debye length defined in terms of the electron and ion Debye lengths  $\lambda_D^{-2} \equiv \lambda_{De}^{-2} + \lambda_{Di}^{-2}$  for the static case, i.e.  $M = 0$ . When charging is only due to plasma currents, the floating potential in a collisionless plasma is typically of the order of  $\Phi_{fl} \approx -2k_B T_e/e_0$ . Thus, from the capacitance model, one can derive a formula for an approximate charge on a negligible small grain with  $a \ll \lambda_D$ :

$$Q_d/e_0 = -1400a_{[\mu\text{m}]}T_{e,[\text{eV}]}, \quad (3)$$

where the grain radius  $a$  is given in micrometers and temperature in eV. In the case of no plasma flow relative to the dust grain, the negatively charged grain is shielded by a stationary, positively charged ion cloud. The electric potential around a small (non-absorbing) charged grain takes the form of a statically screened Coulomb potential, which is typically referred to as the Debye–Hückel or Yukawa potential

$$\Phi_{\text{Yuk}}(r) = \frac{1}{4\pi\epsilon_0} \frac{Q_d}{r} e^{-\frac{r}{\lambda_D}}. \quad (4)$$

Plasma absorption, ion–neutral collisions and plasma flow can modify the potential distribution. Notably, the long-range asymptote of the plasma-mediated potential is often not screened exponentially, but has a power-law decay instead; see, for example, [33, 53, 54, 67, 68].

Plasma flow breaks the symmetry in the grain charging. In the mesothermal velocity regime, when the flow velocity  $u_i$  is larger than the ion thermal velocity  $v_{T_i}$  but less than the electron thermal velocity  $v_{T_e}$  ( $v_{T_i} < u_i < v_{T_e}$ ), the grain will receive a larger ion flux to the surface on the upstream than on the downstream side, while the electron flux will be similar on both sides. Anisotropic charging can lead to an electric dipole on the grain [30, 66]. The electric dipole moment depends on the material of the grain and is more pronounced for supersonic flows [37]. For small conducting grains the electric dipole can often be neglected, as the charge is redistributed on the surface, but for larger conducting grains, the potential distribution in the vicinity of a grain can modify the charge distribution on the grain surface.

A streaming plasma leads to a wake in the density and potential distributions around the grain. The main mechanisms for the wake formation are plasma absorption on the grain surface and the influence of the electric field on plasma particle trajectories in the vicinity of the grain [41]. Plasma absorption leads to density depletion on the downstream side, while electric fields can scatter ions into the wake region forming the ion focus region. Both effects are more pronounced for cold ions, as well as for supersonic flows, when also a Mach cone forms.

The charging time in a streaming plasma is longer than in a stationary plasma and depends on the material of a dust grain, being longer for insulating grains, for which it can take several ion plasma periods to reach stationary conditions.

## 2. Linear response approach

According to the OCP concept, the multi-component dusty plasma can be reduced to a subsystem of dust grains which interact via a dynamically screened Coulomb potential. This dynamical potential takes into account the effect of plasma streaming on the dielectric response of the plasma. Depending on the quality of the dielectric function  $\epsilon(\mathbf{k}, \omega)$ , the considered dynamical screening model comprises an accurate representation of the most essential plasma properties including screening, wakefield oscillations, ion and electron thermal effects, Landau damping, as well as collisional damping [33, 48].

### 2.1. Theoretical approach

Considering a weak (linear) response of the plasma to the presence of the dust grain, the electric potential can be computed by a 3D Fourier transformation

$$\Phi(\mathbf{r}) = \int d^3\mathbf{k} \frac{Q_d}{2\pi^2 k^2 \epsilon(\mathbf{k}, \mathbf{k} \cdot \mathbf{u}_i)} e^{i\mathbf{k}\mathbf{r}}, \quad (5)$$

where  $\mathbf{r}$  denotes the distance from the grain's center of mass. The (shifted) Maxwellian plasma is represented by the following longitudinal dielectric function, which includes Bhatnagar–Gross–Krook (BGK)-type ion-neutral collisions [69, 70]:

$$\epsilon^l(\mathbf{k}, \omega) = 1 + \frac{1}{k^2 \lambda_{D_e}^2} + \frac{1}{k^2 \lambda_{D_i}^2} \left[ \frac{1 + \zeta_i Z(\zeta_i)}{1 + \frac{iv_{in}}{\sqrt{2}kv_{T_i}} Z(\zeta_i)} \right], \quad (6)$$



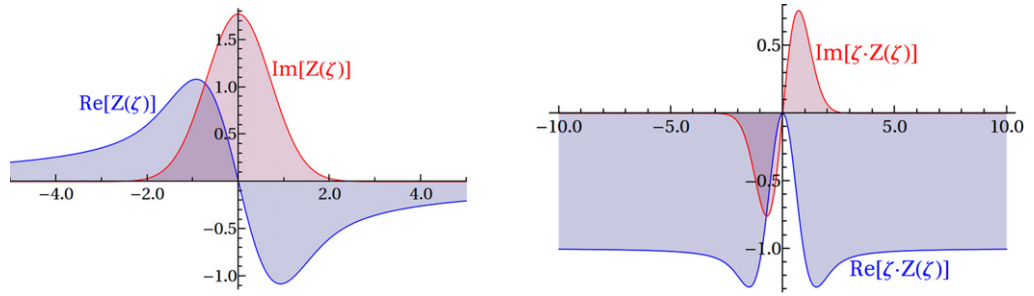


**Figure 2.** Real and imaginary parts of the plasma dispersion function  $Z(\zeta)$  for a real  $\zeta$  (left) and the product  $\zeta \cdot Z(\zeta)$  (right), which enters equation (6).

where we use the substitution

$$\zeta_i = \frac{\mathbf{k}(\mathbf{v}_d - \mathbf{u}_i) + i\nu_{in}}{\sqrt{2}kv_{T_i}}. \quad (7)$$

The screening by electrons is considered as static (Yukawa-type), since the electron flow is of no relevance ( $u_e \ll v_{T_e}$ ). The plasma dispersion function is defined as

$$Z(\zeta) = \frac{1}{\sqrt{\pi}} \int_{-\infty}^{\infty} \frac{\exp(-t^2)}{t - \zeta} dt = i\sqrt{\pi} \exp(-\zeta^2) \text{Erfc}(-i\zeta). \quad (8)$$

The function  $Z(\zeta)$  and the product  $\zeta \cdot Z(\zeta)$  are plotted in figure 2. In the limiting case of  $M = 0$ , that is,  $(\mathbf{v}_d - \mathbf{u}_i) \rightarrow 0$ , equation (6) reduces to static electron and ion shielding, which corresponds to the spherically symmetric Yukawa potential equation (4). For  $|\mathbf{v}_d - \mathbf{u}_i| \gg v_{T_i}$  the product  $\zeta_i \cdot Z(\zeta_i)$  approaches  $-1$  such that the ion-screening contribution vanishes and only electron screening remains in equation (6); see the right panel of figure 2. The finite electron contribution ensures the numerical convergence of the Fourier integral equation (5).

## 2.2. Numerical implementation

The accuracy of the dynamical screening model depends crucially on the 3D discrete Fourier transform (DFT), equation (5). A sufficient sampling rate in  $k$ - and  $r$ -space at the same time requires a large number of sample points, which are, however, in 3D typically limited by computer resources to  $N_x = N_y = N_z = 256$ . Even with the optimal choice of the sampling interval, corresponding to the grid spacing in the reciprocal space, the result for many of the relevant plasma parameters is often not satisfying and lacks accuracy. In particular, the cutoff error in the streaming direction may lead to pseudoperiodicity effects from the DFT, such as artificial oscillations in the upstream direction.

A straightforward approach to reduce the numerical complexity of the Fourier integral equation (5) is to make use of the axial symmetry in the streaming direction by introducing cylindrical coordinates. However, the numerical evaluation of the resulting radial Hankel transform is very time-consuming and converges poorly due to an oscillating Bessel function in the integrand. Instead, an alternative approach was used here to improve the memory and time efficiency by exploiting the radial symmetry. The 3D integration area was sliced along the  $k_z$ -direction and  $N_z$  2D-DFTs were performed on a  $k_{x,y} = 256 \times 256$  grid. Notably, for each  $k_z$ -value only the resulting  $N_x/2 = 128$  values in one radial direction (we used the positive half



of the  $x$ -axis) have to be stored and used for the subsequent  $k_z$ -integration. Hence, instead of  $N_x \cdot N_y = 256^2$ , only  $N_x/2 = 128$  DFTs in the  $k_z$ -direction have to be computed. Moreover, using this scheme the integration area can be easily adjusted to asymmetric spatial dimensions. In particular, for  $M \geq 0.5$  in the case of weak Landau and collisional damping, we used  $N_z = 512$  instead of  $N_z = 256$  grid points, which considerably reduced the pseudoperiodicity effects and ensured convergence of  $\Phi(\mathbf{r})$ .

For the sake of completeness, we should mention that because of different length scales of the Debye potential and the wake modulations we did not transform  $\Phi(\mathbf{k})$  directly, but the difference  $\Delta\Phi(\mathbf{k}) = \Phi(\mathbf{k}) - \Phi_{\text{Yuk}}(\mathbf{k})$  [46], where  $\Phi_{\text{Yuk}}(\mathbf{k})$  denotes the collisionless static case. Subsequently, utilizing the linearity of the Fourier transform, the Yukawa potential equation (4) is added in real space again. In real space, the DFT yields a grid resolution of  $\lambda_{D_e}/8$  for the wake contribution  $\Delta\Phi(\mathbf{r})$ . The data are post processed with a spline interpolation.

In order to ensure the convergence of the Fourier integration, sufficient collisional and/or Landau damping is required. More specifically, for the collisionless case ( $v_{\text{in}} = 0$ ) the temperature ratio is limited to  $T_e/T_i \leq 25$ . For reliable results over the full range of  $M$  and temperature ratios up to  $T_e/T_i = 100$ , weak collisional damping  $v_{\text{in}} = 0.1\omega_{p_i}$  is required. The Fourier integration performs better for small values of  $M$ .

### 2.3. Results

The LR calculations discussed here use the plasma parameters (electron temperature, density, ion mass, etc) as introduced in section 1.1. Neglecting the dust drift, i.e.  $|\mathbf{v}_d| = 0$ , the only dust parameter which enters the calculations is the grain charge, which is set to  $Q_d = -10^4 e_0 = -1.602 \times 10^{-15}$  C. Since the wake potential of a point-like grain ( $a/\lambda_{D_e} \simeq 0$ ) scales linearly with  $Q_d$ , a pre-computed potential  $\Phi(\mathbf{r})$  can easily be adapted to any other grain charge required; see equation (5).

Figure 3 shows the shape of the dynamically screened (wake) potential  $\Phi(\mathbf{r})$  in real space for a range of typical plasma parameters taken from the experiments [8, 23]. To capture the general trends, we consider three characteristic electron-to-ion temperature ratios  $T_r = T_e/T_i = 10, 30, 100$  (top to bottom row) and drift velocities in the subsonic regime ( $M = 0.5$ , left), at the Bohm speed ( $M = 1.0$ , middle column) and supersonic ion flow ( $M = 1.5$ , right). The ion-neutral scattering frequency is fixed at a value of  $v_{\text{in}}/\omega_{p_i} = 0.1$ . According to equation (1) this corresponds to pressures of  $p = 31, 18$  and  $10$  Pa for  $T_r = 10, 30, 100$ , respectively. The plasma flow gives rise to an oscillating wake structure downstream of the grain. On account of that, the grain potential  $\Phi(\mathbf{r})$  essentially deviates from the static Yukawa potential in all considered cases. Typically, the potential's anisotropy, i.e. the symmetry breaking, increases with  $M$ . The wakefield is most pronounced for large values of  $T_r$ .

For  $M = 0.5$  and  $T_e/T_i = 10$  ( $p = 31$  Pa), the range and height of the wakefield oscillations are strongly reduced by the overlapping effect of Landau and collisional damping. Only a relatively weakly pronounced primary potential maximum, i.e. a single node directly behind the grain, emerges in the subsonic regime.<sup>7</sup> For  $M = 1.0$ , and even more pronounced for  $M = 1.5$ , the wave front becomes cone-shaped. In the supersonic case, the peak is lower than

<sup>7</sup> Compared to an isotropically screened Yukawa system, even a relatively shallow wake, such as observed for  $M = 0.5$  and  $T_r = 10$ , was recently shown to have a drastic effect on the collective many-particle behavior [52]. Note that the non-reciprocity of the grain interaction along the streaming direction causes a violation of Newton's law that action equals reaction; see, for example, [48].

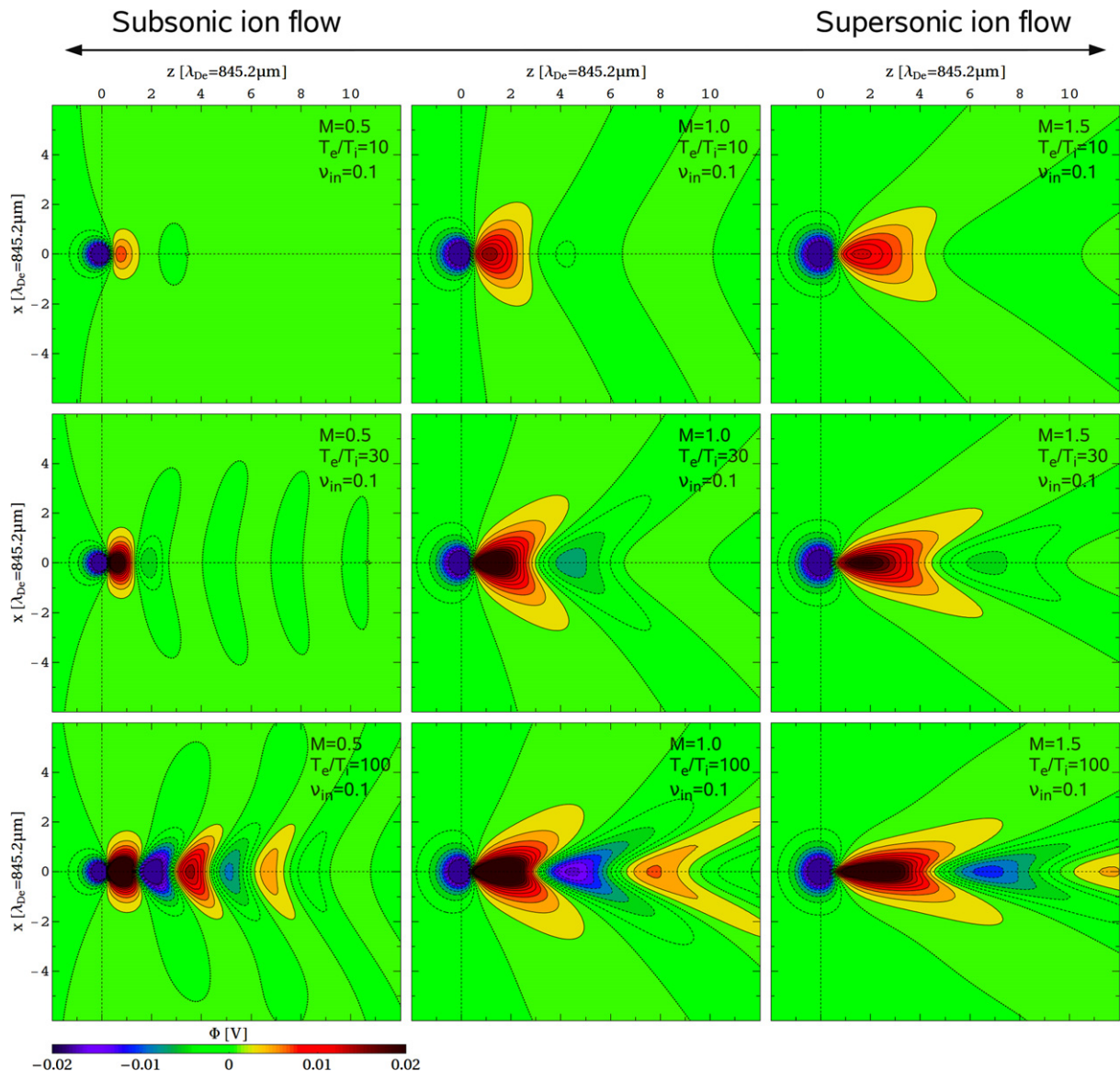


**Figure 3.** Linear response results: contour plots of the grain potential  $\Phi(\mathbf{r})$  for varied streaming velocities  $M = 0.5, 1.0, 1.5$  (from left to right) and electron-to-ion temperature ratios  $T_e/T_i = 10, 30, 100$ , that is,  $T_i = 3000$  K,  $1000$  K,  $300$  K (from top to bottom). The dust grain is placed at the origin and the plasma flows in the positive  $z$ -direction. The ion-neutral collision frequency is fixed at  $\nu_{in}/\omega_{pi} = 0.1$ . Dashed blue (solid red) contours denote areas of negative (positive) space charge; potential values larger than  $20$  mV are clipped and shown in black. The dotted line (on green ground) corresponds to  $\Phi = 0$ . The equipotential lines are separated by  $2$  mV.

for  $M = 1.0$ . The same is observed for the second (third) potential peak for  $T_r = 30$  ( $T_r = 100$ ). Further maxima and minima besides the first downstream potential maximum start to appear for temperature ratios  $T_r > 10$ . Considering  $T_r = 100$ , there are in total three (significant) positive

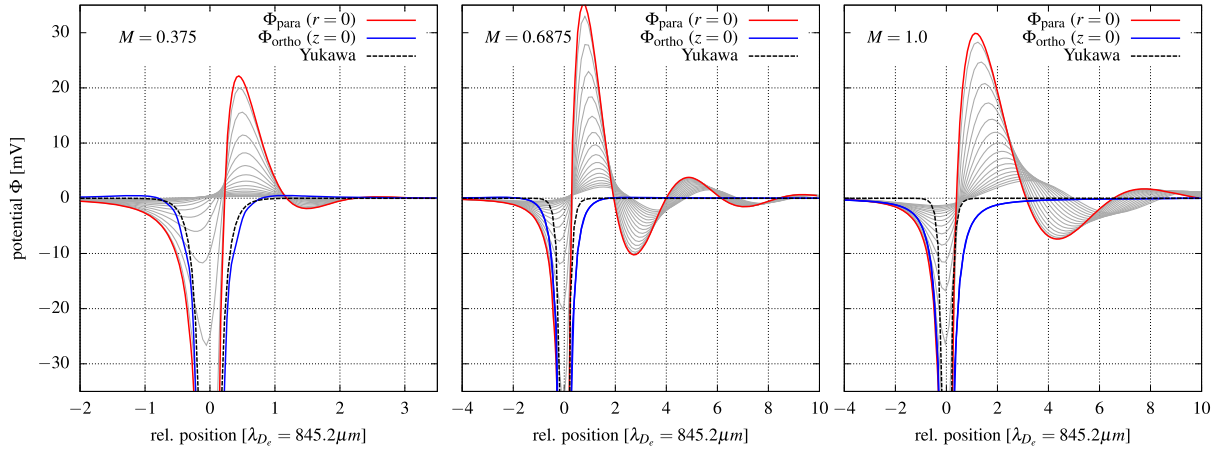


**Figure 4.** LR results for the electrostatic grain potential in the streaming direction  $z$  at  $x = y = 0$  (red) and perpendicular to the flow at  $z = 0$  (blue) for  $M = 0.375, 0.6875$  and  $1.0$  (left to right panel). The dashed black lines indicate the (isotropic) Yukawa potential, equation (4), for the corresponding total Debye length  $\lambda_D = 0.8452$  mm. The light gray curves represent slices through the potential surface in the  $z$ -direction for  $y$ -values in the range  $0 < y \leq 2\lambda_{D_e}$ . Considered parameters:  $T_r = 30$  and  $v_{in} = 0.1\omega_{p_i}$  (cf the middle row in figure 3). Note the different scaling of the abscissas; the range of the ordinate is  $[-35 \text{ mV} : 35 \text{ mV}]$ .

space charge regions, which may result in an attractive (non-reciprocal) force between the equally charged dust grains. For  $M = 1.0$  the form of the wake extends far in the cross-streaming direction. With growing  $M$  the wake becomes increasingly stretched in the streaming direction while the peak height goes down. A plane  $\Phi = 0$  wave front is observed for  $M \approx 0.875$  ( $T_r = 30$ ).

The potential profile can be studied in more detail in figure 4, where cuts through the potential surface are plotted for  $M = 0.375, 0.6875, 1.0$  and  $T_r = 30$ . For the considered grain charge of  $Q_d = -10^4 e_0$  the potential height takes a value around  $10^{-2} k_B T_e / e_0 \approx 25$  mV, which is consistent with [22, 42]. Evidently, an oscillatory wake is not only formed when the speed of the ion flow exceeds the ion-acoustic velocity [54, 71]. Rather, a significant ion focus with a potential peak height of 21.7 mV is already found for  $M = 0.375$ , i.e. well below the ion sound speed. In fact, the highest amplitude of the wakefield is reached at  $M = 0.6875$ ; see also figure 5. In the upstream direction, the range of  $\Phi_{para}$  is already significantly enhanced for  $M = 0.375$ , while in the cross-stream direction  $\Phi_{ortho}$  is still relatively close to the corresponding Yukawa potential for that value. When  $M$  is increased, the (predominantly repulsive) potential profiles in the upstream and cross-stream directions approach each other, as discussed in the context of equation (9).

In the following, we will discuss the functional characteristics of the wakefield downstream from the grain. The potential peak height and its position as a function of  $M$  are plotted in figure 5. The positions of the maxima and minima of the wake potential are found to shift linearly away from the grain when  $M$  is increased. Averaging over the three temperature ratios  $T_e/T_i = 10, 30, 50$  the best linear fit  $a_i M + b_i$  for the  $i$ th peak is obtained for the parameters

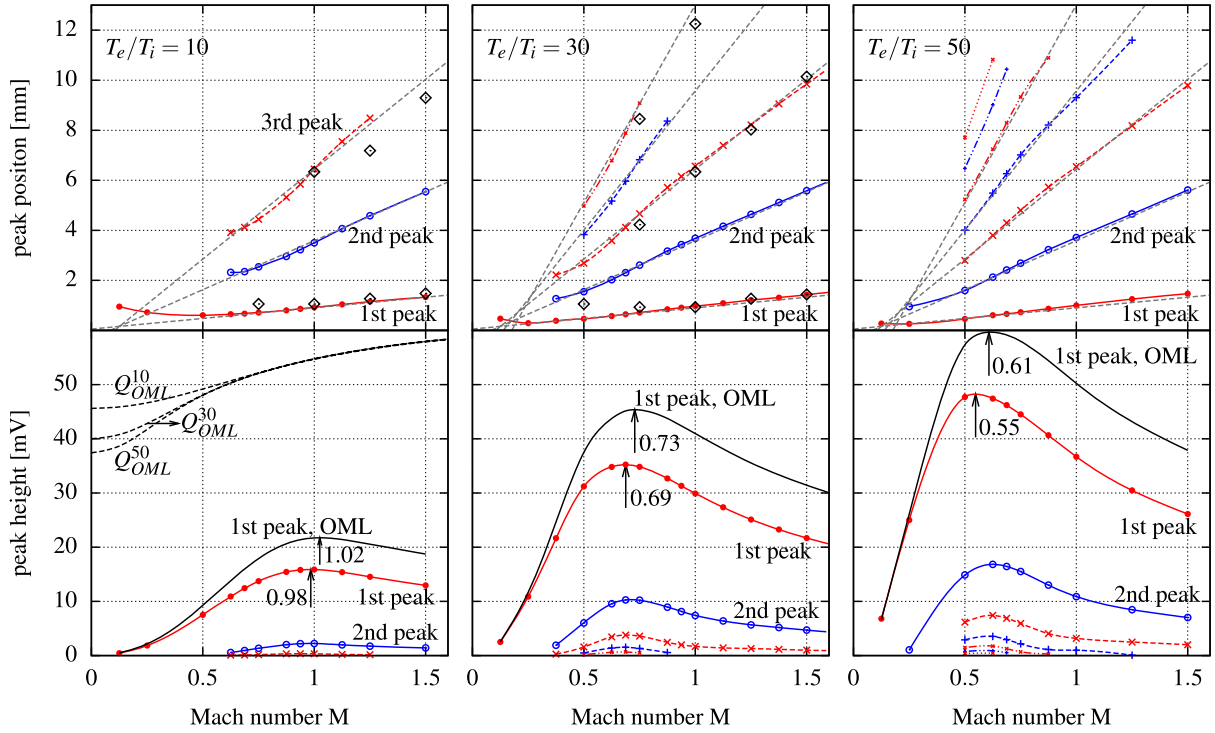


**Figure 5.** Peak positions (top) and peak amplitude (bottom) of the wake potential for  $T_e/T_i = 10, 30, 50$  (from left to right panel) as a function of the Mach number  $M$ . Red (blue) curves correspond to a positive (negative) space charge. The data points are interpolated by splines. In the top (bottom) panel, the peaks in the wake are counted from the bottom (top) curve up (down). The PIC results from table 1 for the wake maxima are denoted by diamond symbols. The dashed black curves in the bottom left panel indicate the charge variation with  $M$  for  $T_r = 10, 30, 50$  according to OML theory (in arbitrary units). The black solid curves (bottom) indicate the height of the first peak in the wake when the effect of charge variation is included.

$a_i = (0.848, 3.91, 7.19, 11.1, 15.8)$  mm and  $b_i = (0.0553, -0.327, -0.745, -1.54, -2.78)$  mm; see dashed gray lines in figure 5 (top). Corresponding PIC results for the wake maxima (see table 1 in section 3) are shown with diamond symbols. Despite the finite and relatively large grain size considered in the PIC simulations, there is good agreement between both methods. On the basis of that result, a longitudinal wavelength of the wake equal to  $2\pi\lambda_{D_e}M$ , discussed in [42], holds in the relevant range of  $M$  as a reasonable approximation.

In figure 5, we also show the magnitude of the potential peak heights as a function of  $M$ . As discussed in the context of figure 4, the wake amplitude reveals a clear maximum when  $M$  is varied. Interestingly, this maximum shifts to the subsonic regime when the ratio  $T_e/T_i$  is increased (in figure 5, an arrow indicates the spline interpolated maximum). According to the OML theory [72], the dust charge  $Q_{OML}^{T_r}$  increases monotonically with  $M$  for the considered velocities, as shown for three temperature ratios in the bottom left panel of figure 5 (see the dashed black curves). Taking the charge increase into account, the maximum value of the peak height shifts to slightly higher values of  $M$  as displayed for the first potential peak (black solid line).

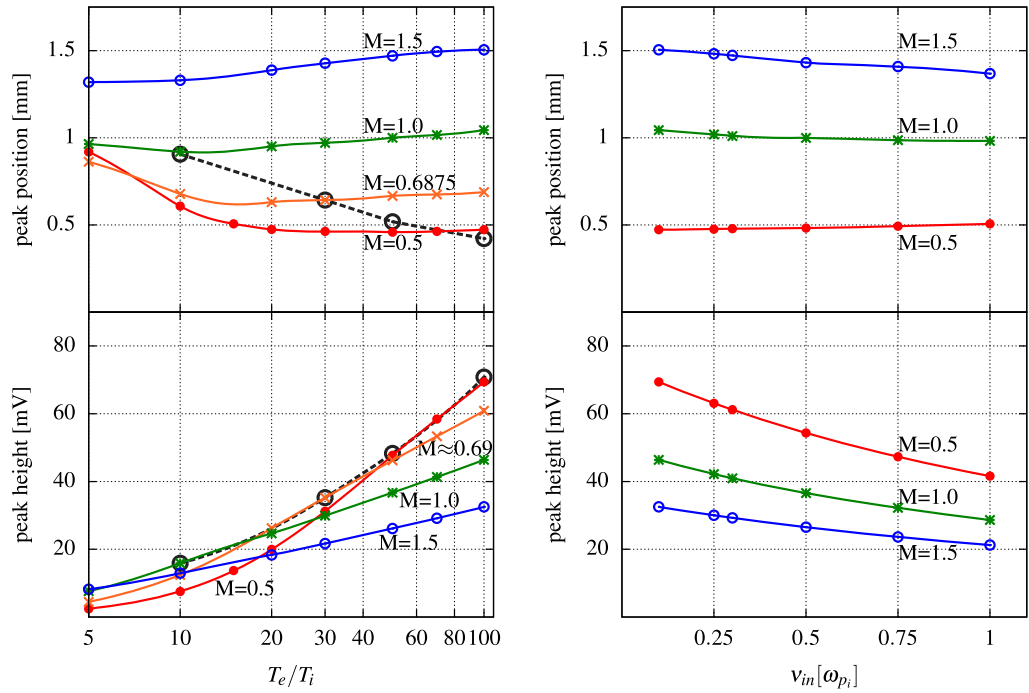


**Figure 6.** Positions (top) and heights (bottom) of the first peak of the wake potential for different  $M$  values as a function of the temperature ratio  $T_e/T_i$  (left panel,  $\nu_{in} = 0.1$ ) and collision frequency  $\nu_{in}$  (right panel,  $T_e/T_i = 100$ ). The data points are denoted by symbols and interpolated by splines. Open black circles mark the absolute maximum of the peak height as a function of  $M$  (bottom left), cf figure 5, and its position (top left) for different ratios of  $T_r$ .

The left panel of figure 6 shows the temperature dependence in more detail. For high ion temperatures, i.e.  $T_r \leq 5$ , the largest peak amplitude is found in the supersonic regime, i.e.  $M \geq 1.5$ . An increase of  $T_r$  leads to a monotonic rise of the potential height (the effect of Landau damping is reduced). The greatest slope of the peak height with respect to  $T_r$  is observed for  $M = 0.5$ . So that in the limit of a large temperature ratio (a low ion temperature), the largest wake amplitude is found in the subsonic regime, that is,  $M = 0.5$ , whereas for the largest Mach number,  $M = 1.5$ , the amplitude of the wake oscillation is considerably smaller. The maximum value of the first peak's height as a function of  $M$  and its position are denoted by open black circles for  $T_r = 10, 30, 50, 100$ . The spline through these data points reveals that the strongest first peak in the wake (the primary potential maximum) over the full range of Mach numbers shifts with an increase of  $T_r$  closer to the dust grain (top left panel). We note that a similar trend as that observed for the fixed grain charge (black dashed line), is found when one includes the effect of the charge increase according to OML theory (not shown). The right panel of figure 6 shows that an increase of ion-neutral scattering  $\nu_{in}$  leads to an increased damping of the wake oscillation with the peak positions being changed only slightly.

So far, we have mainly focused on the potential's wake. The form of the potential upstream and laterally from the grain can be captured by an effective screening length [33, 36, 70, 73, 74]. Figure 7 displays the Debye length as a function of  $M$  for different temperature ratios  $T_r$ . For low ion drift,  $u_i \ll v_{Ti}$ , both electrons and ions provide shielding, but ion screening typically



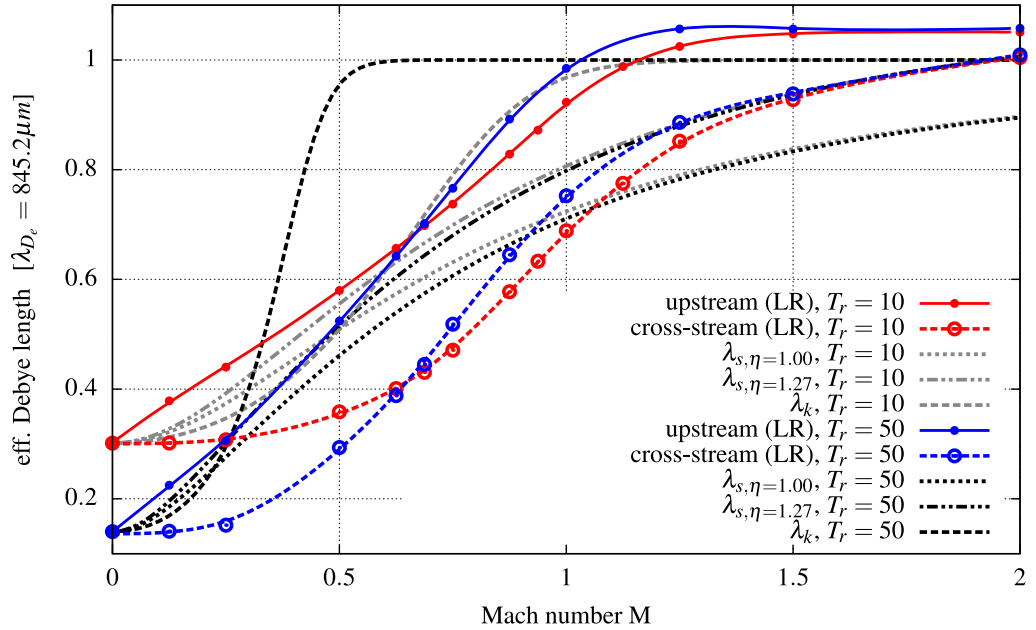


**Figure 7.** LR results for the effective screening length in the upstream (solid) and the cross-stream (dashed) direction relative to the grain as a function of the ion flow velocity  $M$ . The LR results are given for two temperature ratios  $T_r = 10$  (red) and  $T_r = 50$  (blue). The light gray (black) lines indicate the characteristic screening length  $\lambda_s$ , equation (9), for  $\eta = 1.0, 1.27$ , and  $\lambda_k$ , equation (10), for  $T_r = 10$  ( $T_r = 50$ ), respectively.

dominates since  $T_i < T_e$ . For zero flow,  $M = 0$ , the isotropic Yukawa potential, equation (4), applies with the total Debye length being  $\lambda_D = 0.30, 0.14$  in units of  $\lambda_{D_e}$  for  $T_r = 10, 50$ , respectively. In the static case, the negatively charged (Coulomb) potential of the dust grain is predominantly screened by a positively charged ion cloud, which isotropically forms around the grain. In contrast, in the supersonic limit  $M \gg 1$ , (isotropic) Debye screening is entirely contributed by the electrons<sup>8</sup>. For finite  $M$ , the characteristic screening length is found to be different in the upstream and cross-stream directions, with the screening in the upstream direction being larger; see figure 7. It needs to be mentioned that the characteristic screening lengths were obtained by fitting the analytic Yukawa potential to potential cuts through the dust grain as shown in figure 4. However, these potential cuts do not exactly match the functional form of the Yukawa potential. For instance, for  $M = 0.375$  (left panel in figure 4) it is found that the orthogonal slice slightly overshoots  $\Phi = 0$ , i.e. the potential possesses a weakly attractive branch side ways from the grain<sup>9</sup>. Therefore, the screening lengths in figure 7 cover the form of the potential close to the grain, but have an approximate character only. Also, a systematic error is observed in the limit  $M \rightarrow \infty$ , where the value of the effective screening length in the upstream direction converges toward a value that is about 5% larger than the appropriate screening length, that is, the electron Debye length  $\lambda_{D_e}$ . In general, we find that the Yukawa

<sup>8</sup> See also the discussion of equation (6) in section 2.1.

<sup>9</sup> The attractive part is found in a small parameter range only. In experiments and PIC simulations, this weakly pronounced effect has not been observed so far [73].

potential matches the potential profile perpendicular to the flow essentially better than in the upstream direction, which is in agreement with [73].

Finally, we wish to point out that the characteristic screening length can be roughly approximated by the interpolation formula

$$\lambda_s = \lambda_{D_e} \left( \frac{k_B T_i + \eta m_i u_i^2}{k_B T_e + k_B T_i + m_i u_i^2} \right)^{1/2} = \left( \frac{1}{f_s(\eta) \lambda_{D_i}^2} + \frac{f_s(1)}{f_s(\eta) \lambda_{D_e}^2} \right)^{-1/2}, \quad (9)$$

where  $f_s(\eta) = 1 + \eta M^2 \frac{T_e}{T_i}$  and  $\eta$  is a heuristic fitting parameter which we introduce here. Considering  $\eta = 1$ ,  $\lambda_s$  reproduces both screening limits correctly: (i)  $\lambda_s = \lambda_D$  for  $M = 0$  and (ii)  $\lambda_s = \lambda_{D_e}$  for  $M \rightarrow \infty$  (see the dotted lines in figure 7) [36]. However,  $\lambda_s$  is found to converge much more slowly toward  $\lambda_{D_e}$  than the curves obtained by LR theory (figure 7) and PIC simulations (as will be shown in section 3.3, figure 11). Therefore, it is suitable to introduce the fitting parameter  $\eta = 1.27$ , which allows for an essentially better agreement with the present results in the relevant range  $0 \leq M \lesssim 2$ .<sup>10</sup> The concept of an effective screening length in a plasma with streaming ions has been also discussed by Khrapak *et al* ([74] and p 45 of [5]). Here, the analytical form of the effective screening length is approximated by the formula

$$\lambda_k = (f_{1(2)}(M_T) \lambda_{D_i}^{-2} + \lambda_{D_e}^{-2})^{-1/2}, \quad (10)$$

where the two fitting functions  $f_1 = \exp(-M_T^2/2)$  and  $f_2 = (1 + M_T^2)^{-1}$  are defined in terms of the *thermal* Mach number  $M_T \equiv u_i/v_{T_i} = M c_s/v_{T_i}$ . Evidently, with the fitting function  $f_2$ , equation (10) is identical to equation (9) with  $\eta = 1$  and is therefore not further considered in the following. For  $T_r = 10$ , equation (10) yields in conjunction with  $f_1$  a very reasonable approximation (especially for the screening in the upstream direction) without any heuristic parameter; see dashed gray line in figure 7. Furthermore,  $\lambda_k$  shows (in contrast to  $\lambda_s$ ) the correct analytic trend of a rapidly increasing slope with increasing temperature ratio  $T_r$ , which is evident in the intersection of curves at different temperatures. However,  $\lambda_k$  overestimates the decay of the ion contribution to the screening as shown for  $T_r = 50$  in figure 7 and for  $T_r = 30$  in figure 11.

The theoretical finding that the effective screening length converges toward the electron Debye length  $\lambda_{D_e}$  as  $M$  increases is supported by experimental results [75, 76]. In those experiments the effective screening length for the grains suspended in the sheath was found by analyzing collisions between the dust grains. In both cases it was shown that supersonic ions are unable to screen the dust particles and therefore the electron Debye length is the appropriate screening length for dust grains in supersonic plasma flows.

### 3. Three-dimensional particle-in-cell simulations

The LR theory employed in the previous section neglects some important processes associated with the dust grain charging and wake formation. In particular, in the regime of strong plasma flows and high grain charges, nonlinear effects can be significant. Particle kinetic simulations, such as the PIC method, allow for self-consistent studies of the grain charging, and account also for nonlinear phenomena.

<sup>10</sup> At larger values of  $M$ , screening by the electrons plays a dominant role and the effective screening length is therefore close to  $\lambda_{D_e}$ .



### 3.1. Theoretical approach

Analytical plasma models that also account for nonlinear effects are difficult to develop [77]. Therefore, one often employs numerical kinetic particle simulations, in which plasma particle trajectories are followed in self-consistent force fields without many approximations, allowing for a self-consistent evolution of the system. As plasma particle trajectories are the characteristics of the Vlasov equation, the PIC simulations can be considered as an alternative way of solving the Vlasov equation for arbitrary particle distributions [78].

Plasma simulations, in which forces are evaluated between all pairs of simulation particles, are typically very expensive in terms of computational time and memory. A simulation of  $n$  particles, with such direct force calculations, has complexity  $\mathcal{O}(n^2)$ , as approximately  $n^2$  equations need to be solved to find the forces on all the particles.  $\mathcal{O}$  relates to the computer resources usage time. As the number of simulated particles needs to be large, especially in 3D simulations, such an algorithm would be very inefficient.

Introducing a grid within the PIC scheme can significantly reduce the complexity of the algorithm [79]. In the PIC method, the physical quantities of each simulation particle are weighted to neighboring grid points to build appropriate density fields on the grid. In the electrostatic approximation, the electric potential is found from the charge density on the grid points by solving the Poisson equation. Thus, the complexity of the PIC algorithm is  $\mathcal{O}(n) + \mathcal{O}(n_g \log(n_g))$ , where  $n_g$  denotes the number of grid points with  $n_g \ll n$ .  $\mathcal{O}(n_g \log(n_g))$  is the complexity of solving the field equations.

Integration of particle trajectories puts limits on PIC simulations. With both electrons and ions simulated, the time resolution should be a fraction of the electron plasma period. The charging time is usually of the order of the ion plasma period and thus requires a large number of time steps. Simulations can be accelerated by assuming Boltzmann-distributed electrons, which leads to a hybrid PIC–fluid code [80]. This approximation is, however, not always valid, as trapped electrons or electron sources (e.g., due to photoemission) can give rise to local deviations from the Boltzmann distribution [81]. Another way of speeding up the evolution of the system is by using a reduced ion mass  $m_i$ , as the ion plasma frequency increases with a decrease in  $m_i$ . Ion mass values as low as  $m_i = 30m_e$  have been used in the literature [82]. In [37], it has been demonstrated that mass ratios  $m_i/m_e > 100$  give reliable results for dust charging. While the reduction of ion mass leads to some quantitative differences, the results are qualitatively correct and scalable and can be presented in normalized units. Note that with the ion mass being reduced, the sound speed  $c_s$  is increased and the floating potential is slightly reduced. In turn, with a relatively large grain, the discreteness noise and charge fluctuations on the grain are diminished.

### 3.2. Numerical implementation

In the present study, we use the DiP3D (dust in plasma 3D) PIC code, which has been developed to study the charging of dust grains and other objects in various plasma environments [41, 51]. The code simulates a collisionless plasma in the electrostatic approximation, with electrons and ions represented as individual plasma particles. To weight particle charges to the regular grid and to project forces from the grid to the particles, first order linear weighting is used. The particle trajectories are advanced with the *leap frog* method characterized by a staggered time

mesh [79]:

$$\begin{aligned} x_i(t + \Delta t) &= x_i(t) + v_i(t + \Delta t/2)\Delta t, \\ v_i(t + \Delta t/2) &= v_i(t - \Delta t/2) + f_i(t)\Delta t/m_i, \end{aligned} \quad (11)$$

where  $i$  refers to an electron or ion,  $f_i$  is the force projected on the  $i$ th particle from the nearest grid points and  $\Delta t$  is the computational time step. The plasma particles are initially uniformly distributed with Maxwellian velocity distributions in the simulation box of size  $L^3 = (24\lambda_{De})^3$ . The particles are injected into the simulation box at each time step according to the prescribed particle fluxes. To simulate an open plasma system, the particles can leave freely through the boundaries of the simulation box. The code uses the Dirichlet boundary conditions for the potential. The potential at the boundaries is set according to the plasma potential  $\Phi_{pl} = 0$  V.

One or more spherical dust grains are placed inside the simulation domain far away from the boundaries. We assume a conducting grain, and each plasma particle that hits the surface is removed and contributes to the current to the grain. The charge of the removed particle is distributed on the grain surface to cancel internal electric fields. The grain is initially uncharged and becomes charged self-consistently during the simulation.

The DiP3D code is run on a computer cluster, with typically  $n = 10^7$  or more simulation particles distributed on several nodes, with a typical grid size of  $n_g \geq 128^3$ . The message-passing-interface (MPI) is used for parallelization. The code can be stopped and then restarted with modified dust grain configurations. This feature is used to reduce the computation time in the case of systematic parametric studies. The code allows also for movement of the simulated object and for the inclusion of various charging processes such as photoemission. Recently, the code was upgraded to include external magnetic fields and ion–neutral and electron–neutral collisions [83]. With all these features, the code can be placed among other cutting-edge particle plasma codes for object–plasma interactions [36, 56, 84]. In this work, we make use of only the basic features of the code.

It should be noted that the dimensionality of the code is an important aspect of any simulation. For the ultimate goal of direct application of the numerical results to support laboratory studies, 3D simulations should be used. Many important effects, such as ion focusing, are still present when the dimensionality is reduced. However, in a 2D system, the charge of the plasma particle corresponds to the charge of an infinite rod, and a simulated circular grain represents an infinite cylinder. The plasma frequency  $\omega_p$ , Debye length  $\lambda_D$  and charge density do not change with the dimensionality of the system. Reducing the dimensionality can give faster algorithms, but while the results of such simulations are qualitatively correct, they do not need to represent a 3D system quantitatively. Thus, the results from codes with reduced dimensionality should be compared with the corresponding theoretical models. In this paper, we present the results of 3D simulations.

### 3.3. Results

With the DiP3D code, we performed simulations of a single grain in a collisionless plasma. The grain radius is  $a = 0.185\lambda_{De} = 0.1563$  mm. The finite size of the grain leads to enhanced potential variations in the wake as compared to the previous LR results, because the self-consistent grain charge is of the order of  $Q_d \approx -10^5 e_0$ . All other plasma parameters are as described in section 1.1. The grain charging and wake formation have been investigated for different electron-to-ion temperature ratios,  $T_r \in \{10, 30, 100\}$ , and Mach numbers,

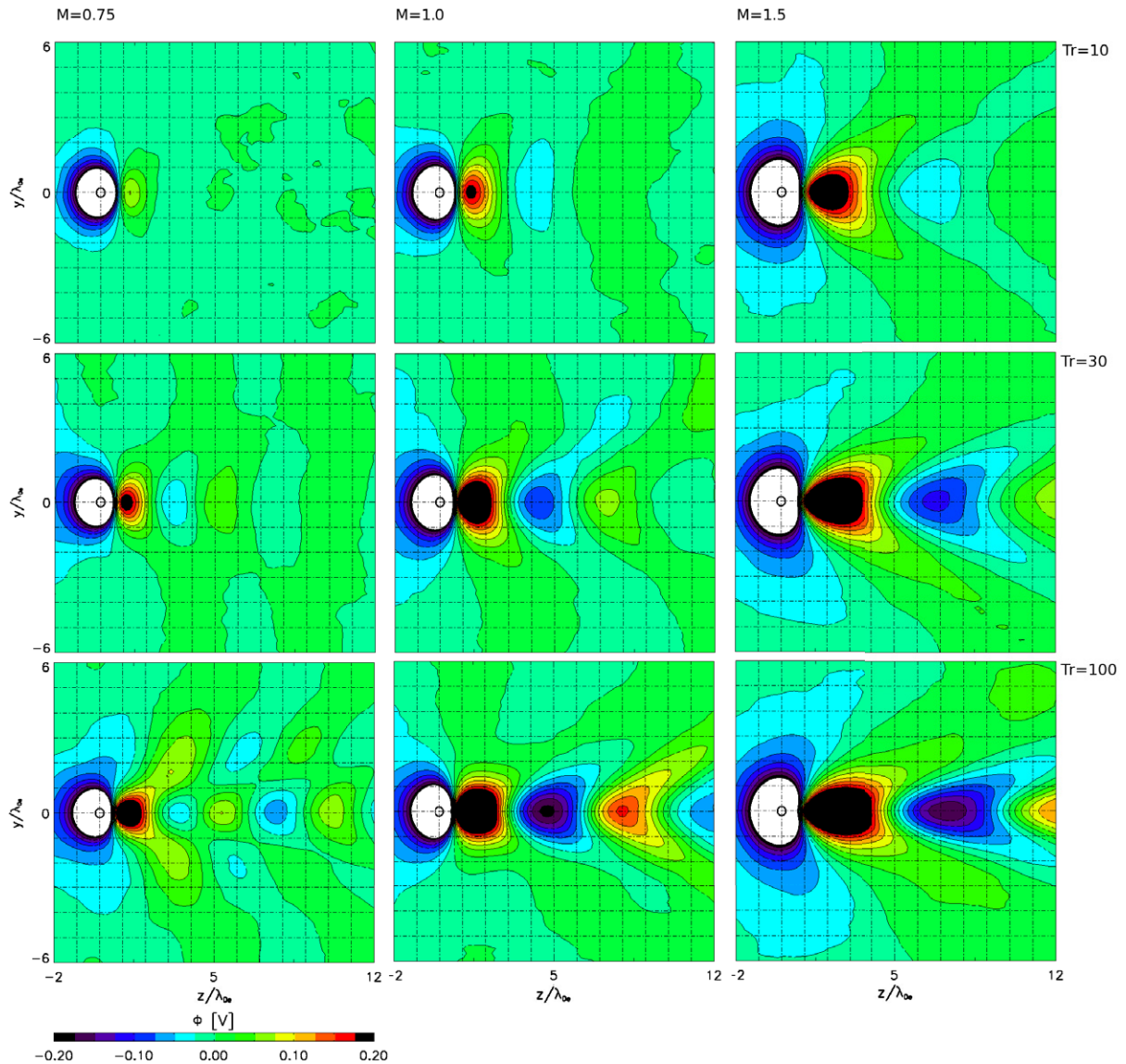


**Figure 8.** First-principles results from collisionless 3D PIC simulations. The contour plots show the wake potential  $\Phi$  in the  $y$ - $z$  plane at  $x = 0$  for varied ion streaming velocities  $M = 0.75, 1.0, 1.5$  (from left to right) along the  $z$ -axis and electron-to-ion temperature ratios  $T_r = 10, 30, 100$  (from top to bottom). The finite-sized dust grain is placed at the origin. Blue (red) codes denote areas of negative (positive) space charge; potential values larger than  $\Phi = 0.2$  V (lower than  $\Phi = -0.2$  V) are clipped and shown in black (white). The size of the dust grain is indicated by the black, open circle at the origin of the coordinate system.

$M \in \{0.75, 1, 1.5\}$ , as shown in the contour plots of the electric potential in figure 8. In all cases, we observe a positive maximum in the potential distribution in the wake at a distance of approximately  $1-2 \lambda_{De}$  downstream from the dust grain. This potential maximum is related to the ion focus in the wake of the negatively charged grain. The maximum in the potential is

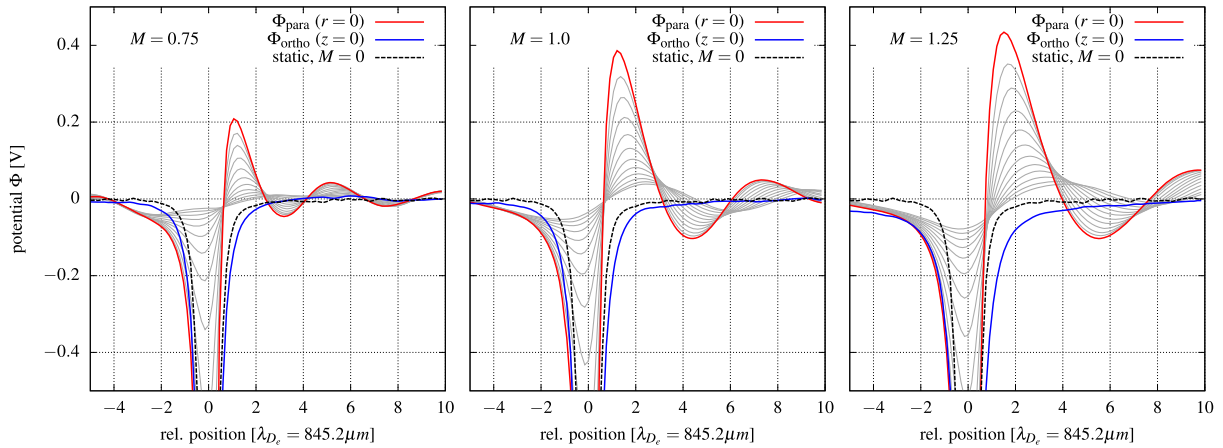


**Figure 9.** 3D PIC results for  $T_e/T_i = 30$ : potential along the flow direction  $z$  through the center of the grain  $x = y = 0$  (red line) and in the cross-stream direction at  $z = 0$  (blue line) for  $M = 0.75, 1.0$  and  $1.25$ . Light gray curves represent slices through the potential surface for  $0 < y \leq 2\lambda_{De}$  (along the direction of the flow). The dashed black line shows the potential drop for the static case,  $M = 0$ , for which  $\Phi_{fl} \sim -2.0V$ . As the floating potential of the grain changes with flow speed, the results for the static case have been rescaled, such that the potential on the grain matches the floating potential on the grain in a flowing plasma.

located further downstream from the grain than the enhancement in the ion density in the focus region, which is consistent with the Poisson equation  $\nabla^2\Phi = -\rho/\epsilon_0$ , where  $\rho$  is the charge density. Ion focusing is due to the deflection of ion trajectories by electric fields in the vicinity of a negatively charged grain [28, 49].

Similarly to the LR results in section 2, in the PIC simulations the potential enhancements in the wake become more pronounced for larger  $M$  and larger electron-to-ion temperature ratios  $T_r$ , i.e. for colder ions. The first local potential maximum is followed by other potential extrema further downstream. For  $T_r = 100$  and  $M = 0.75$ , the pattern in the wake shows a diverse structure with several minima and maxima being also located away from the flow symmetry axis. Note that this could also be an artefact due to the Poisson solver on the finite grid. In particular, for very low  $M$  and  $T_r$ , the possibility for instabilities can become an important issue for the convergence of the code [85]. For larger  $M$  and  $T_r$ , the extrema in the potential distribution are along the direction of the flow. With an increase of the ion temperature, the Landau damping becomes important, and thus ion focusing and wake patterns are less pronounced. For  $T_r = 10$  and  $M = 0.75$ , only a weak, single maximum is observed. The considerable structural consequences of even a weak ion focus were the subject of recent investigations [52].

In figure 9, we present potential cuts along the flow direction  $z$  at  $y = 0$  and  $x \in [0, 2\lambda_{De}]$  for  $T_r = 30$ . In the figure, we also plot the potential cut in the cross-stream direction, as well as the potential cut for the grain in stationary plasma. In contrast with the LR results, the potential maximum monotonically increases with the flow speed, and so does its extension in the

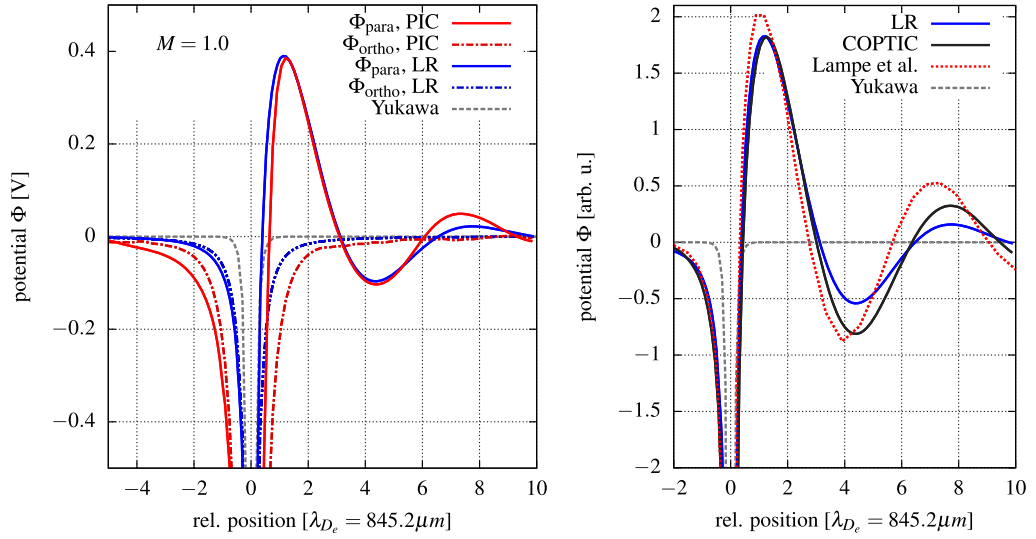


**Figure 10.** Left: potential cuts through the grain along the  $z$ -direction (solid lines) and in the cross-stream direction (dash-dotted lines) for  $M = 1.0$  and  $T_e/T_i = 30$  as obtained from collisionless 3D PIC (red) and LR calculations with  $v_{in}/\omega_{p_i} = 0.1$  (blue). The grain charge of the LR result and the corresponding Yukawa potential are adjusted to match the potential of the PIC simulation, which includes the grain charging process self-consistently. Note that in contrast with PIC, the LR results do not take into account the finite particle radius  $a = 0.185\lambda_{D_e}$ , which explains the offset of the curves. Right: potential cuts along the  $z$ -direction for  $M = 1.0$  and  $T_e/T_i = 50$ . Shown are our LR calculations with finite damping included  $v_{in}/\omega_{p_i} = 0.1$  (blue solid line), COPTIC data obtained by Hutchinson for a point-like grain in a collisionless plasma (black solid line) [42] and LR results for the collisionless case obtained by Lampe *et al* (red dotted line) [33].

perpendicular direction whilst the Mach cone forms. However, there is an important difference between the LR and the PIC results. In the LR analysis, the charge on the grain is constant, whereas in the PIC simulations it changes with the flow. The floating potential on a dust grain in a stationary plasma is  $\Phi_{fl} \sim -2.0$  V and becomes larger with increasing  $M$  (see the discussion below). While the charge and potential on the grain increase with the flow, the amplitude of peaks in the wake potential is being enhanced.

In order to compare the PIC results with LR calculations, in the left panel of figure 10, we present potential cuts through the grain along the  $z$ -direction and in the cross-stream direction for  $M = 1.0$  and  $T_e/T_i = 30$  as obtained from collisionless 3D PIC simulations and from LR calculations with collisional damping included ( $v_{in}/\omega_{p_i} = 0.1$ ). The Yukawa potential, equation (4), for a grain in stationary plasma is also shown. The grain charge of the LR result is adjusted to match the potential of the first peak in the PIC simulation (the same charge is used for the Yukawa potential). It can be inferred from the plot that the agreement between the PIC and LR results is good for the first two extrema. It is important to note that in contrast with the PIC simulations, the LR results do not take into account the finite particle radius  $a = 0.185\lambda_{D_e}$ .



For this reason, the LR curves are slightly shifted toward zero. When the finite size of the grain is taken into account, the agreement between the LR and PIC results for the potential profiles is improved.

As was discussed in the context of figure 5, we observe good overall agreement in the longitudinal wavelength between the PIC and LR results<sup>11</sup>. An essentially larger discrepancy in the wavelengths was recently reported by Hutchinson [42]. Therefore, in the right panel of figure 10 a comparison for  $T_e/T_i = 50$  and  $M = 1.0$  is shown between our LR results, the COPTIC results for a point-like particle (figure 11 of [42]) and the linear calculation by Lampe *et al* (figure 3 of [33]). The main difference between Lampe *et al*'s and our LR results lies in the fact that we include finite collisional damping (which in our case is necessary to avoid pseudoperiodicity effects for the given temperature ratio  $T_e/T_i = 50$ , as stated in section 2.2). The wavelength obtained from COPTIC is in perfect agreement with our LR calculation<sup>12</sup>. The stronger decay of the wake oscillations can be attributed to finite collisional damping which is included in the LR calculations ( $v_{in}/\omega_{p_i} = 0.1$ ). However, in the left panel of figure 5, we observe a much better agreement in the wake amplitude at the first subsidiary valley. The stronger damping in our PIC simulation (left panel) must be due to the large grain size (and charge) giving rise to much stronger nonlinear effects than the point-like grain in the COPTIC simulation. As discussed in [42], a major effect of nonlinearity is the local increase of the effective ion temperature in conjunction with an enhanced Landau damping of the wake amplitude. The presence of (strong) nonlinearities in the present PIC (DiP3D) simulations becomes apparent from the similarity of the shape of the primary potential maximum for  $M = 1$  and the temperature ratios  $T_r = 30$  and especially  $T_r = 100$  (figure 8) and the nonlinear wake structure presented in figure 5(a) in [42]. Therefore, we assume that the good agreement between our collisionless PIC simulation and the LR calculation with collisions included—not only in the wavelength of the wake oscillations but also in the decay of the wake amplitude—is due to a nonlinearity-induced damping mechanism that reduces the amplitude of the wake potential.

In the downstream direction, the primary repulsive branch of the potential is shifted closer toward the grain at finite (subsonic) flows, which is similar to the LR results (cf figures 4 and 9). As ions contribute more to the grain screening in stationary plasma than in flowing plasma, grain screening is strongest in the static (Yukawa) case and weakens for finite  $M$ ; see again figure 9. A quantitative comparison of the PIC and LR results has been made by calculating the effective screening length from the potential profiles for different  $M$  for  $T_r = 30$  in the cross-stream and upstream directions; see figure 11. The general trend of the PIC and LR results is that the effective screening length  $\lambda$  increases with the flow velocity  $M$ . The effective screening for the stationary plasma in the PIC simulations is  $\lambda = 0.23\lambda_{D_e}$ . This value is larger than the results from the LR calculations and also larger than the total Debye length, which is  $\lambda_D = 0.18\lambda_{D_e}$ . The difference is due to a finite grid resolution in the simulation, where the grid spacing is  $\Delta x \approx \lambda_D$ . For flow velocities  $M < 0.5$ , the cross-stream and upstream shielding lengths are less than  $0.4\lambda_{D_e}$ . The values are roughly  $0.1\lambda_{D_e}$  larger (smaller) than the cross-stream (upstream) results from LR calculations. For  $M > 0.5$ , the effective screening length from the PIC simulations strongly increases with  $M$ , with a steeper increase for the upstream

<sup>11</sup> In agreement with [35], the linear approach tends to overestimate the asymmetry of the potential distribution around the dust particle.

<sup>12</sup> Collisional damping has only a minor effect on the peak positions; see the right panel of figure 6.

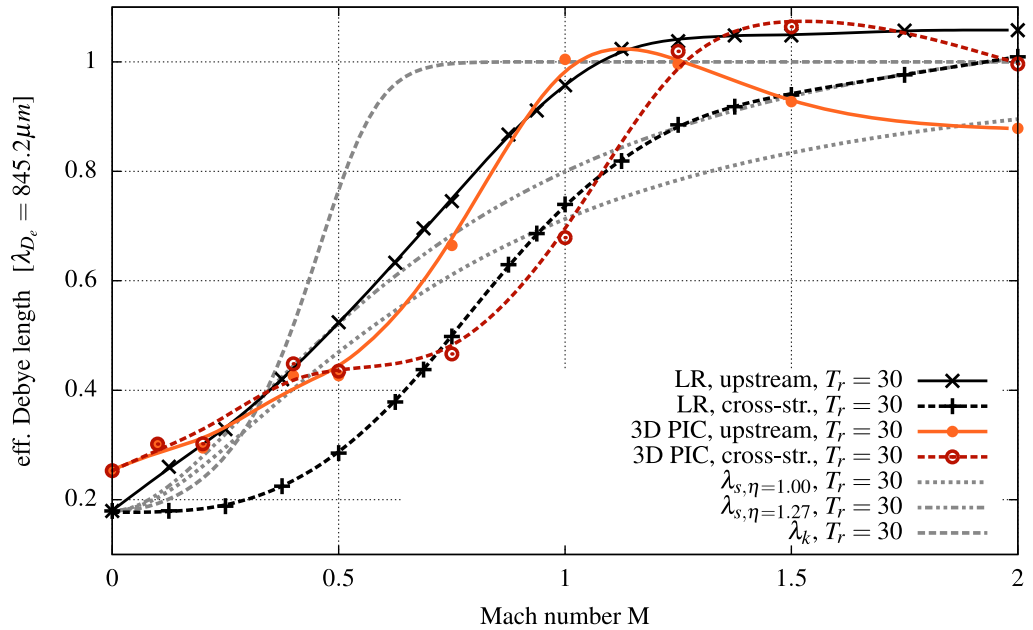


**Figure 11.** Effective screening length of the dust grain potential for  $T_r = 30$  as a function of the ion flow velocity  $M$ . PIC [LR] results for the upstream (solid curve) and the cross-stream (dashed) direction are indicated by circles (crosses) on orange/red (black) lines. These lines are a result of an approximating spline interpolation and therefore do not exactly pass through the data points. The estimated error of the PIC data points is  $\delta \lesssim 0.05\lambda_{D_e}$ . The light gray lines indicate the screening length  $\lambda_s$ , equation (9), for  $\eta = 1.0, 1.27$ , and  $\lambda_k$ , equation (10), respectively. Also see figure 7.

direction. This is the same behavior as for the LR results. At  $M \leq 1$ , for both the LR and the PIC results, the screening length  $\lambda$  is larger on the upstream side than on the downstream side. The increase of the effective screening length with the flow is in agreement with previous studies [33, 70]; however, details of the trend for the cross-stream and upstream directions are different. In [33] the cross-stream shielding was systematically larger than the upstream one. On the basis of our results from simulations with two different numerical methods, the upstream shielding length is larger than the cross-stream one for  $M \leq 1$ . For higher  $M$ , the trend continues for the LR calculations, whereas for PIC simulations, the shielding becomes larger on the cross-stream side than on the upstream side. The effective screening length converges toward the electron Debye length for supersonic flows, as was discussed in the previous section for the LR results.

Finally, in table 1, we summarize the floating potential on the grain as well as the positions and heights of the maxima for different  $M$  values. Since the ion flux to the grain surface changes with the ion flow speed, the floating potential  $\Phi_{fl}$  on the grain becomes more negative with increasing  $M$ . Changing  $T_r$  has little influence on the floating potential, as  $\Phi_{fl}$  is mainly controlled by the electron temperature  $T_e$ , which is kept constant in our simulations. The heights of the potential maxima increase with the flow speed, and so does the distance between the peak and the center of the grain.



**Table 1.** Floating potential  $\Phi_{\text{fl}}$  on the grain and the position  $p_i$  and height  $h_i$  of the  $i$ th maximum in the wake. For some lower velocities only the first maxima were observed. Crosses ( $\times$ ) correspond to possible maxima located outside the simulation domain. The floating potential on the grain in a stationary plasma is  $\Phi_{\text{fl}} \approx -2.6$  V,  $-2.0$  V and  $-1.5$  V for  $T_r = 10, 30, 100$ , respectively. These values agree with the values calculated with the OML theory [72] accounting for the reduced ion mass (reduced  $m_i$  gives less negative  $\Phi_{\text{fl}}$ ; see also section 3.1).

$T_e/T_i = 10$						
M	$\Phi_{\text{fl}}$ (V)	$p_1$ ( $\lambda_{D_e}$ )	$h_1$ (V)	$p_2$ ( $\lambda_{D_e}$ )	$h_2$ (V)	
0.75	-2.8	1.25	0.08	—	—	
1.00	-3.1	1.25	0.195	7.5	0.02	
1.25	-3.4	1.5	0.265	8.5	0.01	
1.50	-3.6	1.75	0.3	11	0.25	

$T_e/T_i = 30$							
M	$\Phi_{\text{fl}}$ (V)	$p_1$ ( $\lambda_{D_e}$ )	$h_1$ (V)	$p_2$ ( $\lambda_{D_e}$ )	$h_2$ (V)	$p_3$ ( $\lambda_{D_e}$ )	$h_3$ (V)
0.50	-2.4	1.25	0.06	—	—	—	—
0.75	-2.8	1.1	0.22	5	0.42	10	0.03
1.00	-3.1	1.1	0.35	7.5	0.6	14.5	0.04
1.25	-3.3	1.5	0.45	9.5	0.75	$\times$	$\times$
1.50	-3.5	1.7	0.45	12	0.65	$\times$	$\times$

$T_e/T_i = 100$					
M	$\Phi_{\text{fl}}$ (V)	$p_1$ ( $\lambda_{D_e}$ )	$h_1$ (V)	$p_2$ ( $\lambda_{D_e}$ )	$h_2$ (V)
0.50	-2.3	1	0.2	3.5	0.1
0.75	-2.8	1.1	0.33	5.5	0.07
1.00	-3.2	1.1	0.55	8	0.165
1.50	-3.8	1.7	0.55	12.2	0.14

#### 4. Method-spanning comparison

We now summarize the correspondence between the two methods and discuss their limitations.

##### 4.1. Comparison of the potentials

The dynamical screening potentials obtained from the LR approach are topologically similar to the corresponding results from the PIC simulations; see again figures 3 and 8. The PIC results are more noisy, as they account for the dynamics of plasma particles and fluctuations in the system. Since the PIC simulations consider a finite-sized grain that is self-consistently charged, the potential on the grain changes with the flow speed; see table 1. A comparison of the peak positions of the positive ion wake charges, figure 5, shows good agreement. Note that the exact position of weak peaks with a low signal-to-noise ratio (high peak numbers at small  $T_r$  and  $M$  values) can barely be resolved; cf figure 3.

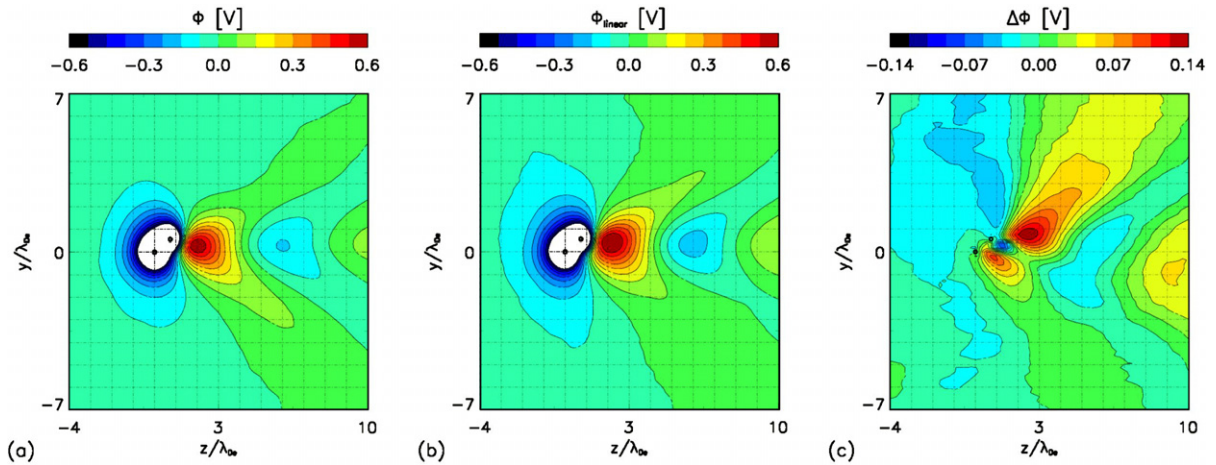


**Figure 12.** (a) Potential around two grains separated by approximately  $\lambda_{D_e}$ , for  $T_e/T_i = 30$  and  $M = 1.25$  obtained by PIC simulations. (b) The potential constructed by a linear combination of the single-grain wake potentials. (c) The potential difference between the constructed potential and the results from the simulation  $\Delta\Phi = \Phi_{\text{linear}} - \Phi$ . Note the different values on the color bars.

The amplitude of the peak in the wake calculated with LR achieves a maximum at a certain ion flow velocity (figure 5). This maximum is at lower flow velocities for larger temperature ratios. We do not see a maximum in the peak amplitude for the PIC results summarized in table 1. However, in section 2, we considered the charge on the grain to be constant, whereas in the PIC simulations the potential on the grain changes with the flow. When scaling linearly all PIC results to a fixed potential, we obtain a maximum in the height of the peak as a function of flow velocity. This maximum is at lower velocities for higher temperature ratios, similarly to the LR results. Moreover, adjusting the correct grain charge, the potential pattern of the wakes obtained from the LR calculations agree well with the PIC results; see again figure 10.

Both LR theory and PIC simulations confirm that the effective screening of the grain changes with the flow. While the effective screening length calculations with the PIC method can be considered to be less accurate due to the potential representation on a finite grid, the trend for the effective screening length agrees with the LR results. For subsonic ion flow velocities, the screening length on the upstream side is usually larger than on the cross-stream side.

#### 4.2. Consideration of shadowing effects

An important question for the OCP model is to determine to what extent the wake potential around two or more grains can be approximated by the linear superposition of single-grain potentials. We will thus study the impact of nonlinear effects in the multiple grain wakes by comparing the results from PIC simulations of two grains with the results obtained by a linear combination of data from the corresponding simulation of a single grain.

In figure 12(a), we show the results from the PIC simulations of two grains for  $T_e/T_i = 30$  and  $M = 1.25$ . The downstream grain is located off the symmetry axis at a distance  $0.93\lambda_{D_e}$  from the upstream grain. The charge of a downstream grain is affected only slightly by the upstream grain, as the downstream grain is located out of the ion focus region [51]. In the linear

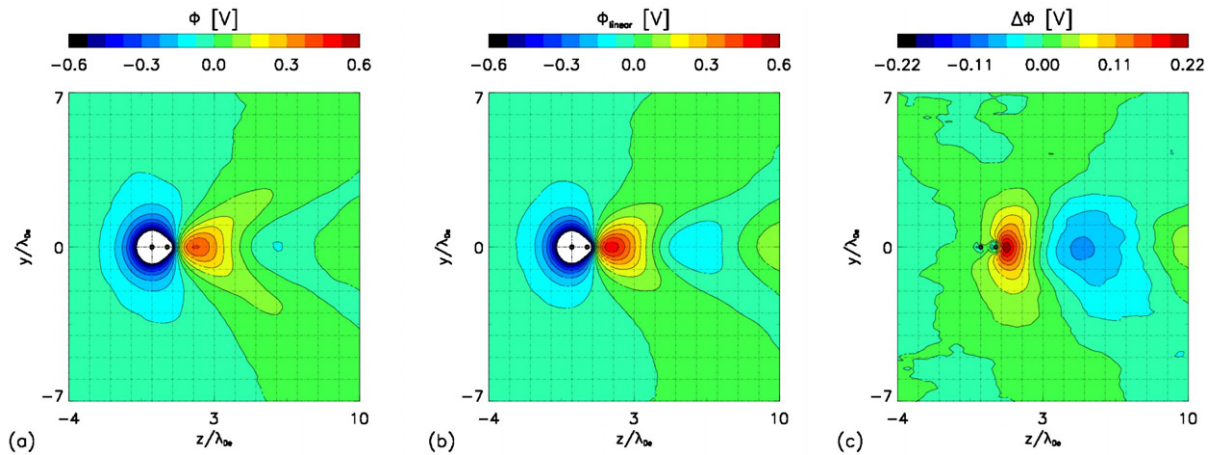


**Figure 13.** The same as figure 12, but for two flow-aligned grains ( $M = 1.25$ ).

combination of two wakes originating from a single-grain calculation, the grain charges (and thus the grain potentials) are adjusted in such a way that they match the corresponding values from the simulations of two grains; see figure 12(b). The constructed wake captures the general features of the results from the simulation of two grains, i.e. the position and approximate height of the potential maxima and minima. However, the small differences between the two results indicate that nonlinear wake effects are present in the simulations of two grains. In figure 12(c), the potential difference  $\Delta\Phi = \Phi_{\text{linear}} - \Phi$  between the linear combination of wakes and the original result is plotted. In the system of two grains, the downstream grain influences the ion dynamics in the wake, and therefore leads to an asymmetric ion focus region, which cannot be fully represented by a linear combination. The potential resulting from the linear combination overestimates the maximum in the wake by up to 20%. Also the symmetry of the wake potential is broken.

The corresponding results for two grains aligned with the flow that are separated by  $0.74\lambda_{De}$  are shown in figure 13. The charge on the downstream grain is strongly affected by ion focusing, and it is only about 30% of the charge on the upstream grain. Thus in the linear combination of the wake, the contribution for the downstream grain has been adjusted accordingly. The constructed wake again represents well the topology of the wake from the simulations of two grains. In this case, the relative potential difference is up to 30% with the strongest discrepancies associated with the first maximum.

The agreement between the constructed and the simulated wake is worse for subsonic flows. Figures 14 and 15 show the corresponding results for the subsonic case  $M = 0.75$  for the downstream grain located off axis and aligned with the flow, respectively. In both cases, the differences  $\Delta\Phi$  are up to 50% in the closest vicinity of the grains.

In all considered cases the general features of the wake, such as positions of the maxima, are well reproduced. In the constructed wakes, the heights of the first maximum are overestimated, and for asymmetric grain arrangements, the symmetry of the wake further downstream from the grains is also modified. This is due to a single asymmetric ion focus region forming in a system of several grains with small separation, which are not aligned with the flow. Thus, constructing the wake from the linear combination of two wakes of single grains should be done with care. To construct such a wake it is necessary to know *a priori* the charge or potential

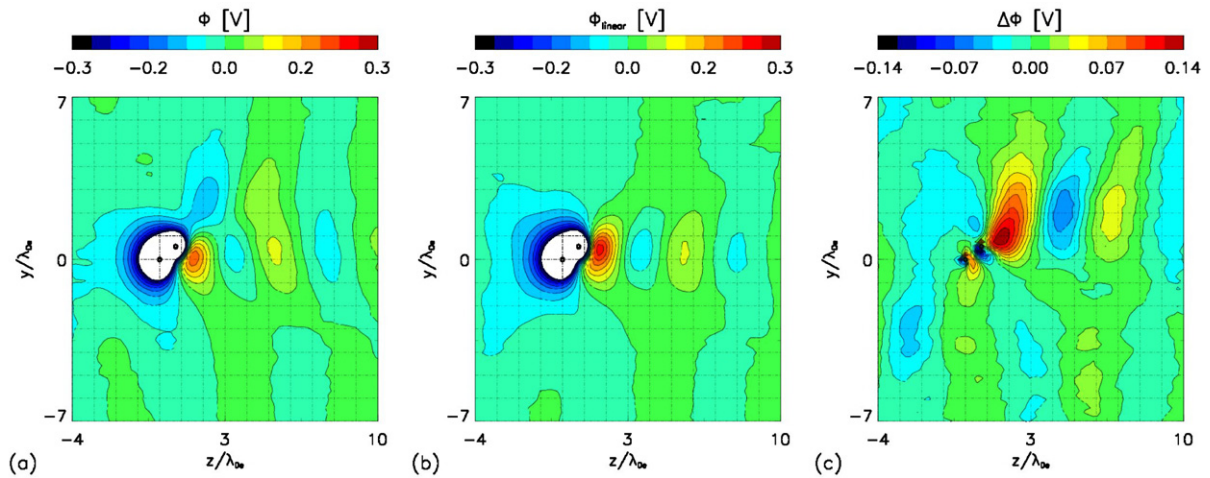


**Figure 14.** The same as figure 12, but for subsonic flow  $M = 0.75$ .

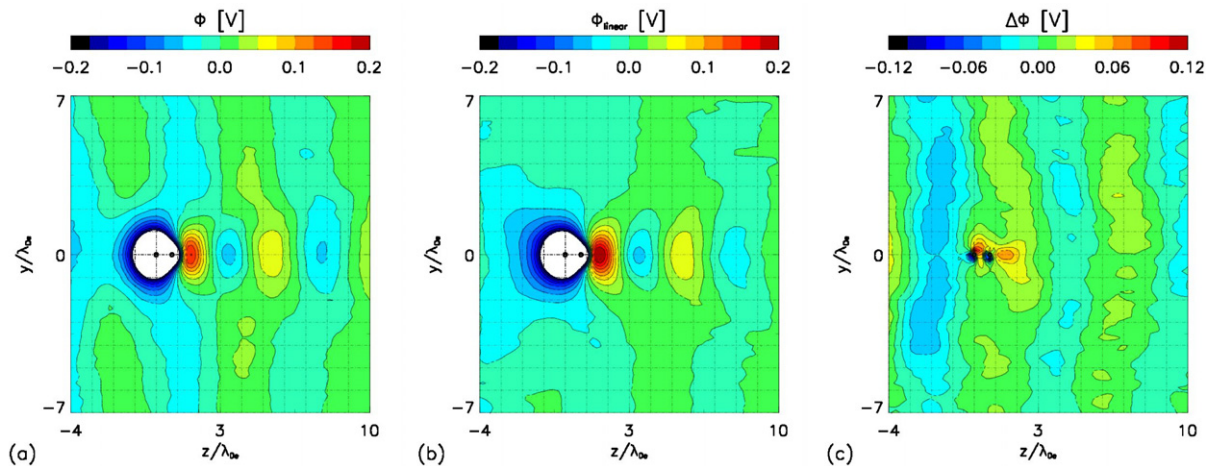


**Figure 15.** The same as figure 12, but for two flow-aligned grains and  $M = 0.75$ .

on a downstream grain, which can be strongly influenced by the wake effects [50, 51]. While the main features of the wake can be well represented by the linear combination of single-grain wakes, there may be inaccuracy due to the nonlinear effects associated with ion focusing.

#### 4.3. Range of applicability of both simulation models

In order to study the wake structure behind a grain in streaming plasmas, we have employed two complementary methods: (i) the numerical evaluation of the linearized electrostatic potential that is created by a point-like charge and (ii) self-consistent, full 3D PIC simulations. These methods have the best performance in different regimes. The LR method has the best convergence for small  $T_r$  and large  $\nu_{in}$  (and of minor importance small  $M$ ), i.e. large Landau and/or collisional dampings are optimal for the performance of the code. The PIC simulations are easiest for higher  $M$  and small  $T_r$ , as the simulations for small  $M$  and cold ions are often favorable conditions for instabilities [85].



In the full PIC method, the ions often have reduced mass. The results with reduced ion mass are reliable when the analysis is carried out in dimensionless units [37]. The PIC method, which includes self-consistent charging of the grain, accounts for a finite grain size, while the LR assumes a point-like dust grain with a given charge. The considered particle radius  $a = 0.185\lambda_{De}$  in the PIC simulations corresponds to the nonlinear regime [42].

The two approaches are complementary and together allow for studies of a grain potential over a wide range of parameters. Moreover, for single-grain simulations, there is good agreement in the functional form of the wake (i.e. the number, shape, height and relative positions of the wake's maxima and minima). The main issue of the LR approach is the correct estimate of the grain charge as a function of  $M$ , and also for a grain that is shadowed by another grain located upstream. A possible solution to overcome this issue could be the use of pre-computed tables obtained from self-consistent PIC simulations or making use of data from experiments [24]. It is also worth mentioning that possible deviations from a shifted Maxwellian ion velocity distribution, as reported in [42, 86, 87], need to be considered in the development of advanced models of the dust plasma interactions applicable for a wide range of plasma parameters.

## 5. Summary and outlook

In this work, we have investigated the electrostatic potential distribution around a spherical dust grain in stationary and flowing plasmas by means of LR calculations and particle-in-cell simulations. The streaming plasma leads to strong deviations from the statically screened Coulomb potential, giving rise to a distinct oscillatory wake structure behind the grain. For both sub- and supersonic flow velocities, positive ion wake charges downstream from the grain are present that can give rise to non-reciprocal dust grain interactions. We have presented a systematic overview of the LR results for different flow velocities, electron-to-ion temperature ratios and ion neutral collision frequencies. The LR results have been tested against self-consistent PIC simulations. The results from the PIC simulations for the wake pattern agree qualitatively with the LR data when the finite size of the grain is accounted for.

Downstream from the grain, a pronounced oscillatory wakefield with several maxima develops with increasing ion flow. Independent of the temperature ratio  $T_e/T_i$ , the peak positions are shifted linearly away from the grain when  $M$  is increased. Upstream and to the side from the grain, the potential decay can be approximated by a Yukawa potential. The effective screening length increases in both directions with the flow, but in contrast with earlier LR results [33], it is found to be larger in the upstream direction than laterally from the grain.

In a system of several grains in a plasma flow, the charge and potential on the downstream grains can be significantly modified by wake effects. The PIC simulations show that the wake behind the two grains can include nonlinear effects and that the charge on the downstream grains can be significantly reduced. While the general wake pattern can be represented by a linear combination of the wake behind a single grain to a rather good accuracy, local deviations up to 50% of the potential are observed for subsonic flows in the closest vicinity of the grains. Thus, special care needs to be taken when applying LR results in OCP simulations, and at least the charge reduction on the downstream grains needs to be considered for the model to be credible.

The influence of wake effects on the collective many-particle behavior in 3D plasma crystals has become a very timely question and is currently under ongoing experimental and theoretical investigations [43–45, 52]. The presented wake potentials are currently employed in

dynamical dust simulations, which accompany the experimental exploration of string formation and externally triggered phase transitions in 3D confined dusty plasma clouds [44, 45]. OCP simulations that include many particles require, however, an adequate adjustment of the charges of the individual grains, which are shadowed by the upstream grains. Such data may be obtained from the first-principles PIC simulations or from experiments [24]. The development of such a grain-charging model is the subject of ongoing work.

Due to the high scalability of Coulomb systems, we expect these results to be of interest also to other types of multi-component plasmas. In particular, the generalization of the dynamically screened dust approach will open up the way to the description of non-equilibrium quantum systems, such as warm dense matter, on the microscopic level. There, the classical dielectric function must be replaced by the corresponding quantum (Mermin) dielectric function [54, 88, 89]. This scheme then allows for the computation of collective many-body properties of strongly correlated ions embedded in a partially ionized quantum plasma of electrons by first-principles molecular dynamics simulations.

## Acknowledgment

The authors thank I H Hutchinson for providing the data for figure 10. This work was supported by the Deutsche Forschungsgemeinschaft via grant LU 1586/1-1 and in part by the Norwegian Research Council, through grant no. 177570.

## References

- [1] Ishihara O 2007 *J. Phys. D: Appl. Phys.* **40** R121
- [2] Bonitz M, Henning C and Block D 2010 *Rep. Prog. Phys.* **73** 066501
- [3] Ludwig P, Thomsen H, Balzer K, Filinov A and Bonitz M 2010 *Plasma Phys. Control. Fusion* **52** 124013
- [4] Merlino R L and Goree J A 2004 *Phys. Today* **57** 32
- [5] Fortov V E, Ivlev A V, Khrapak S A, Khrapak A G and Morfill G E 2005 *Phys. Rep.* **421** 1
- [6] Shukla P K and Eliasson B 2009 *Rev. Mod. Phys.* **81** 25
- [7] Morfill G E and Ivlev A V 2009 *Rev. Mod. Phys.* **81** 1353
- [8] Bonitz M, Horing N and Ludwig P (ed) 2010 *Introduction to Complex Plasmas* (Berlin: Springer)
- [9] Chaudhuri M, Ivlev A V, Khrapak S A, Thomas H M and Morfill G E 2011 *Soft Matter* **7** 1287
- [10] Bonitz M, Block D, Arp O, Golubnychiy V, Baumgartner H, Ludwig P, Piel A and Filinov A 2006 *Phys. Rev. Lett.* **96** 075001
- [11] Donkò Z, Kalman G J and Hartmann P 2008 *J. Phys.: Condens. Matter* **20** 413101
- [12] Henning C, Baumgartner H, Piel A, Ludwig P, Golubnychiy V, Bonitz M and Block D 2006 *Phys. Rev. E* **74** 056403
- Henning C, Ludwig P, Filinov A, Piel A and Bonitz M 2007 *Phys. Rev. E* **76** 036404
- [13] Henning C, Fujioka K, Ludwig P, Piel A, Melzer A and Bonitz M 2008 *Phys. Rev. Lett.* **101** 045002
- [14] Ott T and Bonitz M 2009 *Phys. Rev. Lett.* **103** 195001
- [15] Kählert H and Bonitz M 2010 *Phys. Rev. Lett.* **104** 015001
- [16] Bonitz M, Donkò Z, Ott T, Kählert H and Hartmann P 2010 *Phys. Rev. Lett.* **105** 055002
- [17] Kählert H and Bonitz M 2011 *Phys. Rev. E* **83** 056401
- [18] Ogawa T, Totsuji H, Totsuji C and Tsuruta K 2006 *J. Phys. Soc. Japan* **75** 123501
- [19] Apolinario S W S and Peeters F M 2007 *Phys. Rev. E* **76** 031107
- [20] Takahashi K, Oishi T, Shimomai K, Hayashi Y and Nishino S 1998 *Phys. Rev. E* **58** 7805
- [21] Melzer A, Schweigert V A and Piel A 1999 *Phys. Rev. Lett.* **83** 3194

- [22] Hebner G A and Riley M E 2003 *Phys. Rev. E* **68** 046401  
Hebner G A and Riley M E 2004 *Phys. Rev. E* **69** 026405
- [23] Melzer A, Buttenschön B, Miksch T, Passvogel M, Block D, Arp O and Piel A 2010 *Plasma Phys. Control. Fusion* **52** 124028
- [24] Carstensen J, Greiner F, Block D, Schablinski J, Miloch W J and Piel A 2012 *Phys. Plasmas* **19** 033702
- [25] Saitou Y, Nakamura Y, Kamimura T and Ishihara O 2012 *Phys. Rev. Lett.* **108** 065004
- [26] Vladimirov S V and Nambu M 1995 *Phys. Rev. E* **52** R2172
- [27] Melandsø F and Goree J 1995 *Phys. Rev. E* **52** 5312
- [28] Schweigert V A, Schweigert I V, Melzer A, Homann A and Piel A 1996 *Phys. Rev. E* **54** 4155
- [29] Ishihara O and Vladimirov S V 1997 *Phys. Plasmas* **4** 69
- [30] Lapenta G 1999 *Phys. Plasmas* **6** 1442
- [31] Lemons D S, Murillo M S, Daughton W and Winske D 2000 *Phys. Plasmas* **7** 2306
- [32] Winske D, Daughton W, Lemons D S and Murillo M S 2000 *Phys. Plasmas* **7** 2320
- [33] Lampe M, Joyce G, Ganguli G and Gavrilshchaka V 2000 *Phys. Plasmas* **7** 3851
- [34] Ivlev A V, Khrapak S A, Zhdanov S K, Morfill G E and Joyce G 2004 *Phys. Rev. Lett.* **92** 205007
- [35] Schweigert I V, Schweigert V A and Peeters F M 2005 *Phys. Plasmas* **12** 113501
- [36] Hutchinson I H 2006 *Plasma Phys. Control. Fusion* **48** 185
- [37] Miloch W J, Pécseli H L and Trulsen J 2007 *Nonlinear Process. Geophys.* **14** 575
- [38] Kompaneets R, Vladimirov S V, Ivlev A V and Morfill G 2008 *New J. Phys.* **10** 063018
- [39] Rovagnati B, Lapenta G and Mashayek F 2008 *Phys. Lett. A* **372** 5991
- [40] Guio P, Miloch W J, Pécseli H L and Trulsen J 2008 *Phys. Rev. E* **78** 016401
- [41] Miloch W J 2010 *Plasma Phys. Control. Fusion* **52** 124004
- [42] Hutchinson I H 2011 *Phys. Plasmas* **18** 032111
- [43] Kroll M, Schablinski J, Block D and Piel A 2010 *Phys. Plasmas* **17** 013702
- [44] Schella A, Miksch T, Melzer A, Schablinski J, Block D, Piel A, Thomsen T, Ludwig P and Bonitz M 2011 *Phys. Rev. E* **84** 056402
- [45] Killer C, Schella A, Miksch T and Melzer A 2011 *Phys. Rev. B* **84** 054104
- [46] Joyce G, Lampe M and Ganguli G 2001 *IEEE Trans. Plasma Sci.* **29** 238
- [47] Hammerberg J E, Lemons D S, Murillo M S and Winske D 2001 *IEEE Trans. Plasma Sci.* **29** 247
- [48] Lampe M, Joyce G and Ganguli G 2005 *IEEE Trans. Plasma Sci.* **33** 57
- [49] Miloch W J, Pécseli H L and Trulsen J 2008 *Phys. Rev. E* **77** 056408
- [50] Ikkurthi V R, Matyash K, Melzer A and Schneider R 2010 *Phys. Plasmas* **17** 103712
- [51] Miloch W J, Kroll M and Block D 2010 *Phys. Plasmas* **17** 103703
- [52] Ludwig P, Kählert H and Bonitz M 2012 *Plasma Phys. Control. Fusion* **54** 045011
- [53] Chaudhuri M, Khrapak S A, Kompaneets R and Morfill G E 2010 *IEEE Trans. Plasma Sci.* **38** 818
- [54] Vladimirov S V 2011 *Plasma Phys. Control. Fusion* **53** 074005
- [55] Verboncoeur J P 2005 *Plasma Phys. Control. Fusion* **47** A231
- [56] Matyash K, Schneider R, Ikkurthi R, Lewerentz L and Melzer A 2010 *Plasma Phys. Control. Fusion* **52** 124016
- [57] Naval Research Laboratory (NRL) Plasma Formulary 2009, p 39 (<http://wwwppd.nrl.navy.mil/nrlformulary/>)
- [58] Cramer W H 1959 *J. Chem. Phys.* **30** 641
- [59] Bernstein I B and Rabinowitz I N 1959 *Phys. Fluids* **2** 112
- [60] Goree J 1992 *Phys. Rev. Lett.* **69** 277
- [61] Zobnin A V, Nefedov A P, Sinel'shchikov V A and Fortov V E 2000 *J. Exp. Theor. Phys.* **91** 483
- [62] Lampe M, Goswami R, Sternovsky Z, Robertson S, Gavrilshchaka V, Ganguli G and Joyce G 2003 *Phys. Plasmas* **10** 1500
- [63] Khrapak S A *et al* 2005 *Phys. Rev. E* **72** 016406
- [64] Hutchinson I H and Patacchini L 2007 *Phys. Plasmas* **14** 013505



- [65] Bouchoule A (ed) 1999 *Dusty Plasmas: Physics, Chemistry and Technological Impacts in Plasma Processing* (New York: Wiley)
- [66] Ivlev A V, Morfill G and Fortov V E 1999 *Phys. Plasmas* **6** 1415
- [67] Joyce G and Montgomery D 1967 *Phys. Fluids* **10** 2017  
Montgomery D, Joyce G and Sugihara R 1968 *Plasma Phys.* **10** 681
- [68] Khrapak S A, Klumov B A and Morfill G E 2008 *Phys. Rev. Lett.* **100** 225003
- [69] Alexandrov A F, Bogdankevich L S and Rukhadze A A 1984 *Principles of Plasma Electrodynamics* (Berlin: Springer)
- [70] Jenko F, Joyce G and Thomas H M 2005 *Phys. Plasmas* **12** 022309
- [71] Vladimirov S V, Ostrikov K and Smarian A A 2005 *Physics and Applications of Complex Plasmas* (London: Imperial College Press) p 57
- [72] Fortov V, Iakubov I and Khrapak A 2006 *Physics of Strongly Coupled Plasma* (Oxford: Oxford University Press)
- [73] Konopka U, Morfill G E and Ratke L 2000 *Phys. Rev. Lett.* **84** 891
- [74] Khrapak S A, Ivlev A V, Zhdanov S K and Morfill G E 2005 *Phys. Plasmas* **12** 042308
- [75] Arnas C, Mikikian M and Doveil F 2001 *Phys. Scr.* **T89** 163
- [76] Konopka U, Ratke L and Thomas H M 1997 *Phys. Rev. Lett.* **79** 1269
- [77] Rommel J M and Kalman G 1996 *Phys. Rev. E* **54** 3518–30
- [78] Büchner J 2007 Vlasov-code simulation *Advanced Methods for Space Simulations* ed H Usui and Y Omura (Tokyo: Terrapub)
- [79] Birdsall C K and Langdon A B 1991 *Plasma Physics via Computer Simulation* (Bristol: Adam Hilger)
- [80] Cartwright K L, Verbocoeur J P and Birdsall C K 2000 *Phys. Plasmas* **8** 3252
- [81] Miloch W J, Vladimirov S V, Pécseli H L and Trulsen J 2009 *New J. Phys.* **11** 043005
- [82] Spitkovsky A 2008 *Astrophys. J.* **637** L39
- [83] Miloch W J, Guldbrandsen N, Mishra L N and Fredriksen Å 2010 *Appl. Phys. Lett.* **97** 261501
- [84] Engwall E, Eriksson A I and Forest J 2006 *Phys. Plasmas* **13** 062904
- [85] Brackbill J U 1988 *J. Comput. Phys.* **75** 469
- [86] Schweigert V A 2001 *Plasma Phys. Rep.* **27** 997
- [87] Ivlev A V, Zhdanov S K, Khrapak S A and Morfill G E 2005 *Phys. Rev. E* **71** 016405
- [88] Graziani F R *et al* 2012 *High Energy Density Phys.* **8** 105
- [89] Ludwig P, Bonitz M, Kählert H and Dufty J W 2010 *J. Phys. Conf. Ser.* **220** 012003